

Article

# Study of the Optimal Grid Resolution and Effect of Wave–Wave Interaction during Simulation of Extreme Waves Induced by Three Ensuing Typhoons

Shih-Chun Hsiao <sup>1</sup> , Han-Lun Wu <sup>1</sup> and Wei-Bo Chen <sup>2,\*</sup> 

<sup>1</sup> Department of Hydraulic and Ocean Engineering, National Cheng Kung University, Tainan City 70101, Taiwan

<sup>2</sup> National Science and Technology Center for Disaster Reduction, New Taipei City 23143, Taiwan

\* Correspondence: wbchen@ncdr.nat.gov.tw

**Abstract:** Three typhoons, Meranti, Malakas, and Megi, occurred successively in eastern Taiwanese waters in September 2016, causing extreme waves (significant wave height > 10.0 m), and these events were selected to investigate the effect of model grid resolution and wave–wave interaction on simulating typhoon-driven waves. The WAVEWATCH III (WW3) model, with 0.50 deg, 0.25 deg, 0.20 deg, 0.10 deg, and 0.05 deg grid resolutions, and two reanalysis wind fields were adopted to simulate ocean waves during these three typhoons. The results indicated that the exertion of the Climate Forecast System version 2 (CFSv2) winds over the WW3 model with 0.10 deg grid resolution yielded optimum simulations of typhoon waves in a compromise between accuracy and elapsed time. In the present study, the WW3 model modeled nonlinear wave–wave interactions using discrete interaction approximation (DIA). The numerical experiments revealed that the underestimations of typhoon waves were significant when the WW3 model excluded nonlinear wave–wave interactions, especially when employing a higher grid resolution. This study also found that the WW3 model is superior to the Wind Wave Model III (WWM-III) using the CFSv2 winds because the WWM-III tended to overestimate the extreme waves in all three of these eastern Taiwan typhoon events that occurred in September 2016.

**Keywords:** extreme waves; three successive typhoons; grid resolutions; wind–wave model; intermodal comparison



**Citation:** Hsiao, S.-C.; Wu, H.-L.; Chen, W.-B. Study of the Optimal Grid Resolution and Effect of Wave–Wave Interaction during Simulation of Extreme Waves Induced by Three Ensuing Typhoons. *J. Mar. Sci. Eng.* **2023**, *11*, 653. <https://doi.org/10.3390/jmse11030653>

Academic Editor: Lev Shemer

Received: 20 February 2023

Revised: 15 March 2023

Accepted: 16 March 2023

Published: 20 March 2023



**Copyright:** © 2023 by the authors. Licensee MDPI, Basel, Switzerland. This article is an open access article distributed under the terms and conditions of the Creative Commons Attribution (CC BY) license (<https://creativecommons.org/licenses/by/4.0/>).

## 1. Introduction

Tropical cyclones (typhoons or hurricanes) impact millions of people, resulting in billions of US dollars (USD) of damage every year worldwide. Super typhoons, which are equivalent in strength to an intense Category 4 or Category 5 hurricane, are powerful tropical cyclones that occur in the western North Pacific and rank among the most dangerous global natural hazards [1]. Moreover, extreme ocean surface waves associated with typhoons are among the most severe threats to coastal zones, nearshore waters, and navigational safety [2–9], and with many coastal areas experiencing some of the highest rates of coastal erosion [10], better knowledge of how to accurately predict typhoon-induced storm waves is extremely valuable for disaster prevention. Numerous researchers have conducted studies on multiple-typhoon interactions using numerical models [11–15]; however, few studies have simulated extreme waves caused by successive typhoons. The term successive typhoons refers to the same offshore waters being affected by the former and the latter typhoons simultaneously.

The wind–wave simulation contains two aspects of human knowledge: theory, which addresses basic principles from more fundamental sciences, and practical applications. Ever-increasing human interactions with the sea have offered endless opportunities to apply theoretical knowledge to everyday problems. With rapid advances in scientific

research, wind–wave simulations have utterly matured. More fundamental advances in wave modeling have occurred in the past 60 years, followed by periods involving the application and proliferation of minor-scale improvements [16]. Although high-performance computing facilitates the computational speed of modeling systems, multiple sources of error remain, from model parameters, inputs, and processes to the physical parameterization that accounts for model limitations and simplification. Therefore, determining the damage caused by typhoon-generated waves using wind–wave numerical models requires an evaluation of simulation accuracy [17].

Simulating or predicting realistic storm waves relies highly on numerical efficiency, a state-of-the-art wind–wave model, and a more accurate typhoon wind field [18]. Forcing wind–wave models using gridded meteorological data with high spatial and temporal resolutions, rather than analytical/parametric models, could improve the accuracy of storm wave simulations. Accordingly, the model grid resolution is important for the simulation of typhoon-driven waves, especially for extreme waves exceeding a height of 10.0 m. Worldwide, the scientific community has developed a series of numerical wind–wave models called third-generation wave models, e.g., WAM (WAVE Modeling: Ref. [19]), WW3 (WAVEWATCH III: Ref. [20]), the SWAN model (Simulating Waves Nearshore: Ref. [21]), and WWM-III (Wind Wave III: Ref. [22]), which have been widely applied for global- or regional-scale sea state forecasts. Hence, the intercomparison of wave models is necessary to adopt the optimal wind–wave model to acquire more accurate simulations and forecasts [23].

This paper aims to study the role of grid resolutions and wave–wave nonlinear interactions in storm wave simulations by employing a third-generation wind–wave model and atmospheric forcings from global numerical weather simulation systems. This study reports the importance of wind inputs to a numerical wave model when a typhoon impacts Taiwanese waters and also determines the optimal model grid resolution for forecasting wind waves operationally in Taiwanese waters based on a compromise between the simulation accuracy and elapsed time. Finally, an intercomparison of two third-generation wave models is conducted. This paper is arranged as follows: Section 2 describes the three typhoons that successively impacted Taiwan. The details of the data and model are presented in Section 3, and the results of a series of scenario simulations are given in Section 4. In Section 5, a discussion and intermodal comparisons are presented, and finally, a summary and our conclusions are given in Section 6.

## 2. Three Successive Typhoons That Impacted Taiwan in September 2016

In September 2016, three successive typhoons resulted in severe marine weather in the waters surrounding Taiwan. They approached Taiwan on 12 to 15 September, 15 to 18 September, and 25 to 28 September, and they are known as Meranti, Malakas, and Megi, respectively. The Central Weather Bureau of Taiwan also issued sea and land warnings for these three typhoons in 2016 because of the threats they posed to Taiwan. The history of these three typhoons can be briefly described as follows.

Typhoon Meranti was one of the most intense tropical cyclones on record. Meranti became a tropical depression on 8 September 2016, near the island of Guam, and then subsequently impacted Batanes (a province in the Philippines), Taiwan, and Fujian Province of China, in September 2016. Typhoon Meranti gradually intensified until 11 September, when it entered a period of rapid intensification and became a super typhoon early on 12 September. Meranti passed through the Luzon Strait, reaching its peak intensity on 13 September with 1 min sustained winds of 315 km/h. Typhoon Meranti traveled to the area south of Taiwan as a super typhoon and steadily weakened due to the high mountains in Taiwan. Typhoon Meranti reached Fujian Province as a Category 2-equivalent typhoon on 15 September, and it became the strongest typhoon on record to land in the province. Typhoon Meranti degraded to the extratropical level and finally passed to the south of the Korean Peninsula. The arrival time in UTC and the tracks of Typhoon Meranti are shown in Figure 1a.

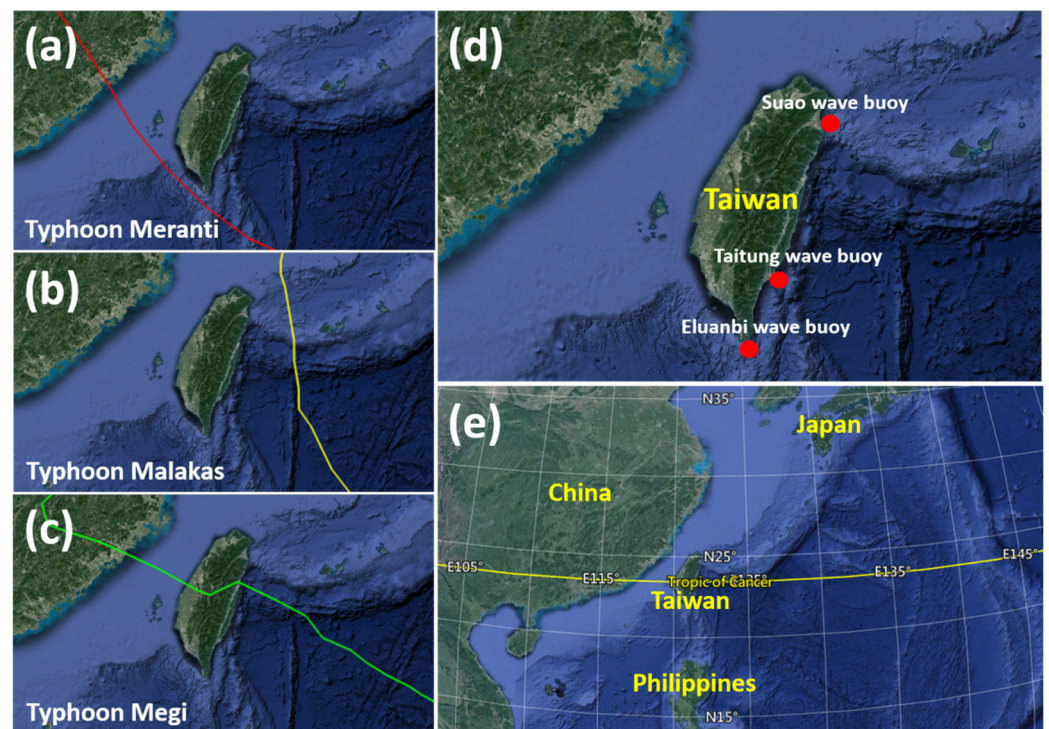


**Figure 1.** Tracks of (a) Typhoon Meranti (12 to 15 September), (b) Typhoon Malakas (15 to 18 September), and (c) Typhoon Megi (25 to 28 September); (d) locations of the wave buoys and (e) the computational domain ( $105^{\circ}$  E– $140^{\circ}$  E,  $15^{\circ}$  N– $32^{\circ}$  N) for the present study.

Typhoon Malakas was upgraded to a Category 2 typhoon on 15 September 2016, and it reached its peak intensity with 1 min sustained winds of 215 km/h and a minimum pressure of 930 hPa. The Japan Meteorological Agency (JMA) recorded 10 min sustained winds of 175 km/h for Typhoon Malakas on 17 September. On 18 September, Typhoon Malakas intensified as it moved east–northeastward and became a Category 3 typhoon on 19 September. Then, Malakas started to weaken due to land interaction with Japan. The Joint Typhoon Warning Center downgraded Typhoon Malakas to a tropical storm on 20 September. The JMA and JWTC issued their final advisories as it became an extratropical system later that day. The tracks and arrival time of Typhoon Malakas are shown in Figure 1b.

Typhoon Megi was a large and powerful tropical cyclone that affected Taiwan and eastern China in late September 2016. The JMA upgraded a tropical depression to a tropical storm, named it Megi early on 23 September, and subsequently upgraded it to a typhoon on 24 September. The JMA indicated that Typhoon Megi reached its peak intensity on 26 September with 10 min maximum sustained winds of 155 km/h and a central pressure of 940 hPa. Typhoon Megi had already intensified into a stronger typhoon before making landfall in Hualien, Taiwan, on 27 September. Typhoon Megi significantly weakened due to interaction with the high mountains in Taiwan. Typhoon Megi entered the Taiwan Strait and landed over Huian in Fujian Province, China, on 28 September. The tracks and arrival times of Typhoon Megi are shown in Figure 1c.

### 3. Data and Model

#### 3.1. Measurements at Wave Buoys

The significant wave height, mean period, and wave direction recorded by three-wave buoys deployed in the offshore eastern waters of Taiwan were selected to validate the model performance regarding typhoon wave simulation with various grid resolutions. These three-wave buoys are Suao, Taitung, and Eluanbi, from north to south (Figure 1d). The Water Resources Agency (WRA) of Taiwan is responsible for the maintenance and

operation of these three-wave buoys. The WRA indicates that the sampling frequency of their wave buoys reaches 2 Hz over 10 min at the beginning of each hour, and the accuracy of the significant wave height measurement is  $\pm 10$  cm.

### 3.2. Wind Data Input for the Wind–Wave Model

The accuracy of wind input is essential in the simulation and prediction of ocean waves, especially for a typhoon event. The present study utilized two prevalent wind field products that served as the forcing of the wave model and then selected a better wind field from a typhoon wave simulation to conduct subsequent numerical experiments.

ERA5 replaced ERA-Interim in September 2019 and is the latest atmospheric reanalysis dataset produced by the European Centre for Medium-Range Weather Forecasts (ECMWF). The move from ERA-Interim to ERA5 represents a significant improvement in the overall quality and level of detail in the model [24]. Notably, ERA5 has a higher horizontal resolution than ERA-Interim. Hourly reanalysis products are available at a horizontal resolution of  $0.25^\circ$  (approximately 30 km) on 137 vertical levels; however, ERA-Interim has a 75 km resolution and 60 levels for the horizontal and vertical resolutions, respectively. The present study acquired ERA5 hourly 10 m winds from the Climate Data Store.

The Climate Forecast System version 2 (CFSv2) is an upgraded Climate Forecast System (CFS) product that became operational at the National Centers for Environmental Prediction (NCEP) on 30 March 2011 [25]. The CFSv2 is the same model that created the NCEP Climate Forecast System Reanalysis (CFSR); additionally, the CFSv2 dataset is an extension of the CFSR. The CFSv2 products are available at spatial resolutions of  $0.205^\circ$  by  $0.204^\circ$ ,  $0.5^\circ$  by  $0.5^\circ$ ,  $1.87^\circ$  by  $1.904^\circ$ , and  $2.5^\circ$  by  $2.5^\circ$  and at hourly intervals. The present study utilized hourly winds with a specified above-ground height of 10 m and a spatial resolution of  $0.205^\circ$  by  $0.204^\circ$  from the Research Data Archive of the National Center for Atmospheric Research for typhoon wave simulations.

### 3.3. Bathymetric Data Input for the Wind–Wave Model

Detailed bathymetry allows for better simulation of nearshore water physics, such as wave dissipation and three-wave interactions (i.e., triads). The General Bathymetric Chart of the Oceans (GEBCO)\_2022 Grid product is the latest global gridded topographic and bathymetric product that provides global coverage of elevation data in ocean and land regions at a 15 arc-second spatial resolution [26]. The GEBCO\_2022 Grid includes datasets from many international and national data repositories and regional mapping initiatives. The GEBCO includes sparse regional grids for the base grid using a remove–restore blending procedure. The present study interpolated the GEBCO\_2022 grid into the WAVEWATCH III (WW3) model with various grid resolutions.

### 3.4. Wind–Wave Model Description and Configurations

This study implemented the WAVEWATCH III (hereafter WW3) model version 6.07 [27] to simulate typhoon-generated wind waves in Taiwanese offshore waters. WW3 version 6.07 is equipped with a new parallelization algorithm, domain decomposition, and an optional implicit numerical scheme for coastal application at high spatial resolution with either unstructured or structured grids compatible with community-based coupling infrastructure [28]. The present study runs the WW3 model with spherical coordinates in its two-dimensional, nonstationary mode. Chen [29] indicated that the offshore boundary far from the study area is essential for accurately simulating typhoon waves. Therefore, the computational domain of the WW3 model ranges from  $105^\circ$  E to  $140^\circ$  E and from  $15^\circ$  N to  $32^\circ$  N (Figure 1e) and covers the entire Taiwan Strait, the northwest Pacific, the East China Sea, and the northern South China Sea. This sizeable domain is extensive enough to accommodate typhoons, with a large size traveling long distances from the far field to the near field.

WW3 is a state-of-the-art third-generation spectral wave model that includes options for shallow-water (surf zone) applications and wetting and drying grid points. The WW3

model has been widely used in regional and global wave forecasts/hindcasts, which solve the wave action equation based on the spectral energy balance equation in the Eulerian form [27] for wave propagation, described as follows:

$$\frac{DN}{Dt} = \frac{S}{\sigma'} \tag{1}$$

where  $N$  is the wave action density spectrum,  $t$  is time,  $\sigma$  is the intrinsic (radian) frequency, and  $S$  represents the net effect of sources and sinks on the spectrum, defined as follows:

$$S = S_{ln} + S_{in} + S_{nl} + S_{ds} + S_{bot} + S_{db} + S_{tr} + S_{sc}, \tag{2}$$

where  $S_{ln}$  is a linear input term for providing more realistic initial wave growth,  $S_{in}$  represents an atmosphere–wave interaction term,  $S_{nl}$  expresses a nonlinear wave–wave interaction term,  $S_{ds}$  is a wave breaking dominated wave–ocean interaction term,  $S_{bot}$  represents a wave–bottom interaction term,  $S_{db}$  expresses a wave breaking dominated wave–ocean interaction term,  $S_{tr}$  is a triad wave–wave interaction term that presents parameterization and limited accuracy, and  $S_{sc}$  represents a bottom–feature-induced wave scattering term. The WW3 model solves the spectral wave action balance equation numerically in spherical coordinates:

$$\frac{\partial N}{\partial t} + \frac{1}{\cos \varphi} \frac{\partial}{\partial \varphi} \dot{\varphi} N \cos \theta + \frac{\partial}{\partial \lambda} \dot{\lambda} N + \frac{\partial}{\partial \kappa} \dot{\kappa} N + \frac{\partial}{\partial \theta} \dot{\theta}_g N = \frac{S}{\sigma'} \tag{3}$$

$$\dot{\varphi} = \frac{c_g \cos \theta + U_\varphi}{R}, \dot{\lambda} = \frac{c_g \sin \theta + U_\lambda}{R \cos \varphi}, \dot{\theta}_g = \dot{\theta} - \frac{c_g \tan \theta + \cos \theta}{R},$$

where  $t$  is time;  $\varphi$ ,  $\lambda$ ,  $\kappa$ , and  $\theta$  represent the latitude, longitude, wavenumber, and wave direction, respectively;  $R$  is the radius of the earth;  $C_g$  is the deep-water group velocity; and  $U_\varphi$  and  $U_\lambda$  are current components in the latitude and longitude directions, respectively. Moreover,  $N$  is a function of five variables ( $t, \varphi, \lambda, \kappa, \theta$ ).

The present investigation considered five scenarios with various grid resolutions for the same computational domain (the extent mentioned above). The structured-grid WW3 model with 0.50 deg, 0.25 deg, 0.20 deg, 0.10 deg, and 0.05 deg resolutions was implemented to demonstrate the contribution of grid resolution to the accuracy of typhoon wave simulations. Table 1 lists the number of grid points and elapsed time of a 29-day simulation derived from different mesh resolutions. The simulation period was 1–30 September 2016, which diminishes the influence of the initial conditions on the typhoon-generated waves over the last 20 days (11 to 30 September). More details about the WW3 model configuration for the present study are shown in Table 2.

**Table 1.** The number of grid points and elapsed time of a 29-day simulation for different mesh resolutions used in the numerical investigation.

Model Configuration	Scenarios				
	S1	S2	S3	S4	S5
Mesh resolution	0.50 deg	0.25 deg	0.20 deg	0.10 deg	0.05 deg
Number of grid points	2485	9729	15,136	60,021	239,041
Elapsed time of a 29-day simulation	0.13 h	0.45 h	0.72 h	3.21 h	14.93 h

**Table 2.** Configuration of model parameters for the WW3 model in the present study.

Parameters	Value or Package
Time step	180 s
Number of direction bins	36
Number of frequencies	36
Source term	ST4, Ref. [30] source term package
Wave bottom dissipation	BT1 [31], JONSWAP bottom friction formulation
Depth-induced wave breaking	DB1, Ref. [32] Battjes–Janssen module
Nonlinear wave–wave interactions	NL1 [33], discrete interaction approximation

#### 4. Results

##### 4.1. Accuracy of the Ocean Wave Simulation: Contribution of Wind Input

The ERA5 and CFSR wind fields were linearly interpolated spatially to 0.50 deg, 0.25 deg, 0.20 deg, 0.10 deg, and 0.05 deg to match the spatial resolution of the WW3 model mesh. The output temporal resolution of the WW3 model was set to 3600 s, which is identical to the wind input time step.

The numerical investigation first ran the WW3 model with 0.50 deg grid resolution; moreover, the ERA5 and CFSv2 wind fields from 1 to 30 September 2016 were imposed on the 0.50 deg WW3 model. This simulation scenario was used to evaluate the wind field quality for typhoon-induced storm wave simulation, especially for extreme waves with heights greater than 10 m. Figure 2 contains six snapshots of the spatial distribution of significant wave height driven by Typhoons Meranti (Figure 2a,d), Malakas (Figure 2b,e), and Megi (Figure 2c,f), using the CFSv2 (Figure 2a–c) and ERA5 (Figure 2d–f) winds, respectively. As shown in Figure 2, regardless of whether the wind fields were from ERA5 or CFSv2, the WW3 model reproduced consistent typhoon arrival times and their corresponding center positions, which means that the ERA5 and CFSv2 products are identical regarding the typhoon track. However, apparent discrepancies between ERA5 and CFSv2 exist in the significant wave height simulations when they are used as wind forcings for the WW3 model, and the discrepancy trend is more evident because the typhoon-driven significant wave height is greater.

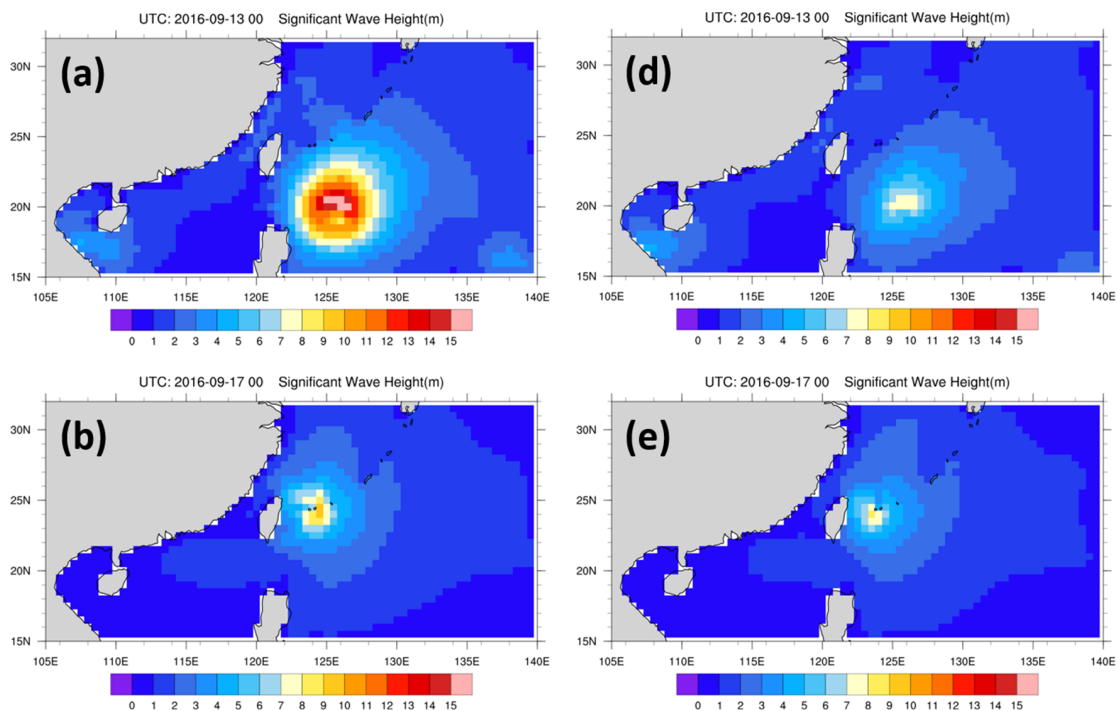


**Figure 2.** Cont.

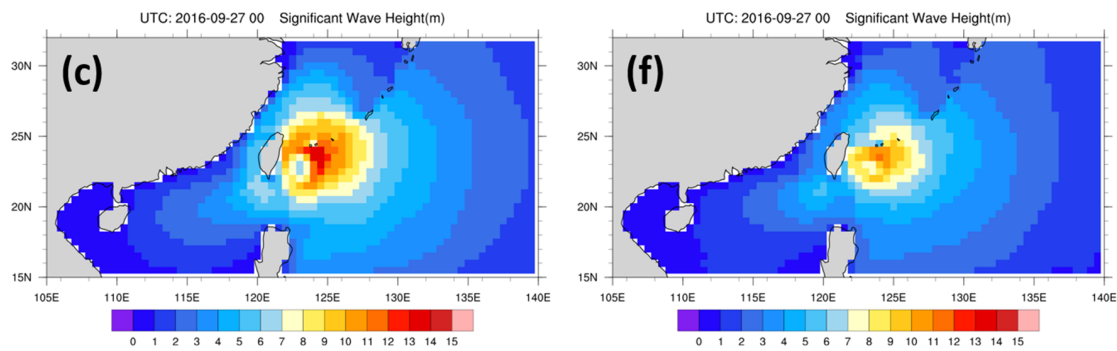


**Figure 2.** Spatial distribution of significant wave height driven by the CFSv2 (a–c) and the ERA5 (d–f) winds; a WW3 model with a 0.50 deg grid resolution was used for Typhoons Meranti (a,d), Malakas (b,e), and Megi (c,f).

Typhoon Meranti was a super typhoon that could instantaneously cause an extremely significant wave height greater than 15.0 m in the deep ocean when imposing the CFSv2 winds on the WW3 model (Figure 2a). Nevertheless, the ERA5 winds only led to approximately 8.0 m of significant wave height (Figure 2d), which is only half the height compared with that observed when using the CFSv2 winds for Typhoon Meranti. Similar phenomena also occurred in simulations of Typhoon-Malakas- and Typhoon-Megi-induced wave height values when using the ERA5 and CFSv2 winds, respectively. The WW3 model paired with the CFSv2 winds could instantaneously simulate 9.0–10.0 m of significant wave height for Typhoon Malakas (Figure 2b). The WW3 model produced a significant wave height of 8.0–9.0 m (Figure 2e) using the ERA5 winds. The wave height difference between the two is only 1.0 m. The ERA5 and CFSv2 winds caused significant wave height simulation discrepancies of 3.0 m in Typhoon Megi, between those of Typhoons Meranti and Malakas. The simulated instantaneous Typhoon-Megi-caused maximal significant wave heights were 14.0–15.0 m (Figure 2c) and 11.0–12.0 m (Figure 2f) using the CFSv2 and ERA5 winds, respectively.

The underestimations of typhoon-generated significant wave height when using the ERA5 winds are not only for the deep offshore ocean two-dimensional contour maps but also for the nearshore individual wave buoy time series. Figure 3 illustrates an hourly significant wave height comparison between the WW3 model simulations and device measurements for the Suao (Figure 3a), Taitung (Figure 3b), and Eluanbi (Figure 3c) wave buoys. The maximal underestimation of significant wave height was 2.0 m at the Suao wave buoy during Typhoon Megi, 10.0 m at the Taitung wave buoy during Typhoon Meranti, and 9.0 m at the Eluanbi wave buoy during Typhoon Meranti (cyan line, Figure 3). The WW3 model with the CFSv2 wind could simulate extremely significant wave heights at the locations of three wave buoys that approached the measurements during the three typhoons (red line, Figure 3); even slight underestimations still exist. An interesting phenomenon of note is that the significant wave height simulations are nearly identical during nontyphoon periods, regardless of whether the ERA5 or CFSv2 winds are used.

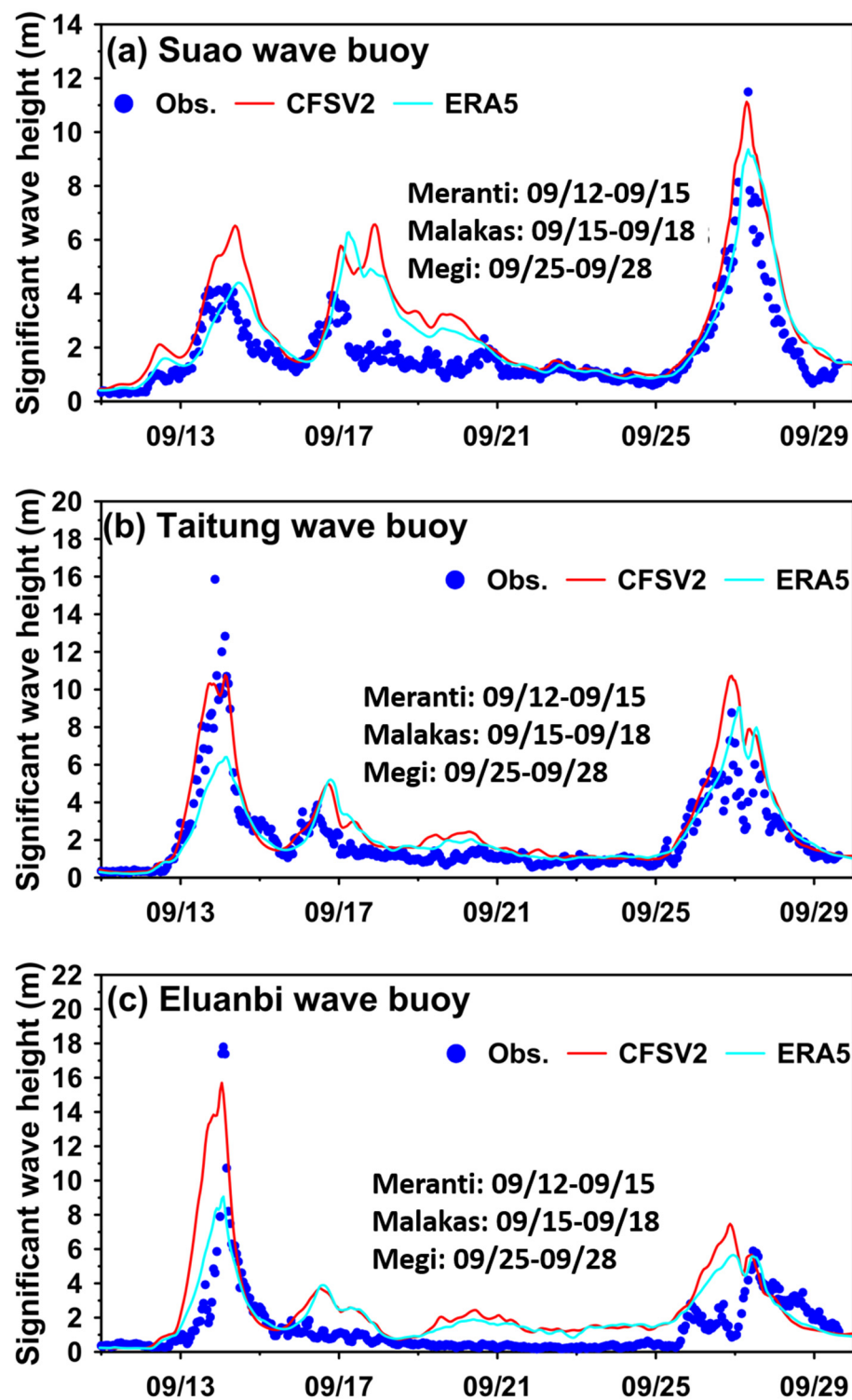
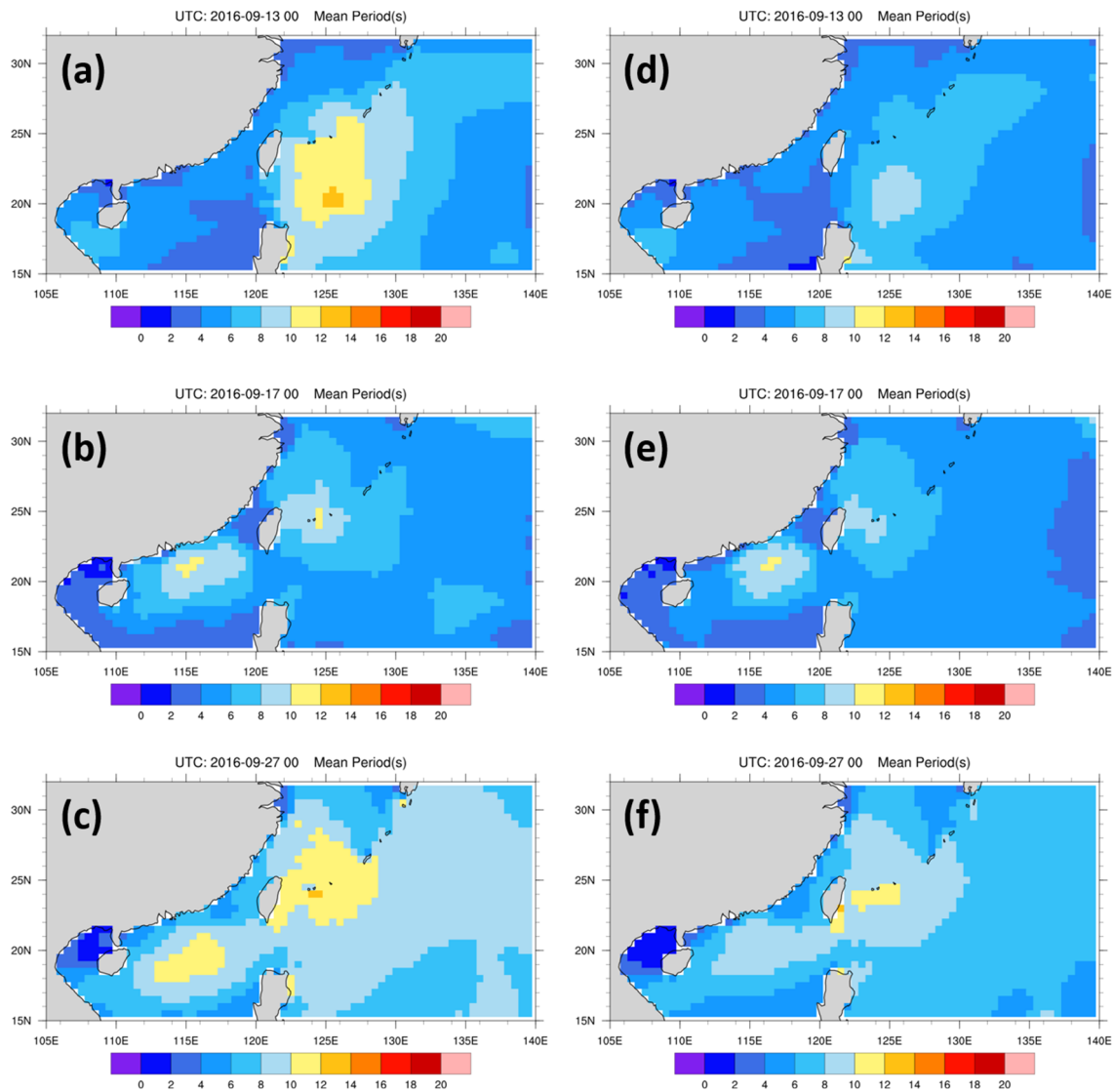


Figure 3. Comparison of the hourly significant wave heights between simulations and measurements for the (a) Suao, (b) Taitung, and (c) Eluanbi wave buoys in September 2016.

The simulations of the mean wave period also reveal the same phenomenon as those of the significant wave height. The CFSv2 winds paired with the WW3 model always produced a mean wave period higher than the WW3 model when employing the ERA5 winds in the deep offshore ocean (Figure 4). They predicted a mean wave period approaching the measurements obtained at the nearshore wave buoys (Figure 5). As the wave direction is periodic between 0°N and 359°N, a quantitative comparison of the model

simulation and buoy measurements is meaningless [34]. Hence, the present evaluation did not create hourly wave direction plots of wave buoys for comparison. However, the CFSv2 wind-driven wave directions were slightly higher than those of the ERA5 winds in degrees (Figure 6). Additionally, Figure 6 shows that the ERA5 and CFSv5 winds produced a similar wave direction pattern in the nearshore waters of Taiwan.



**Figure 4.** Spatial distribution of mean period driven by the CFSv2 (a–c) and the ERA5 (d–f) winds; a WW3 model with a 0.50 deg grid resolution was used for Typhoons Meranti (a,d), Malakas (b,e), and Megi (c,f).

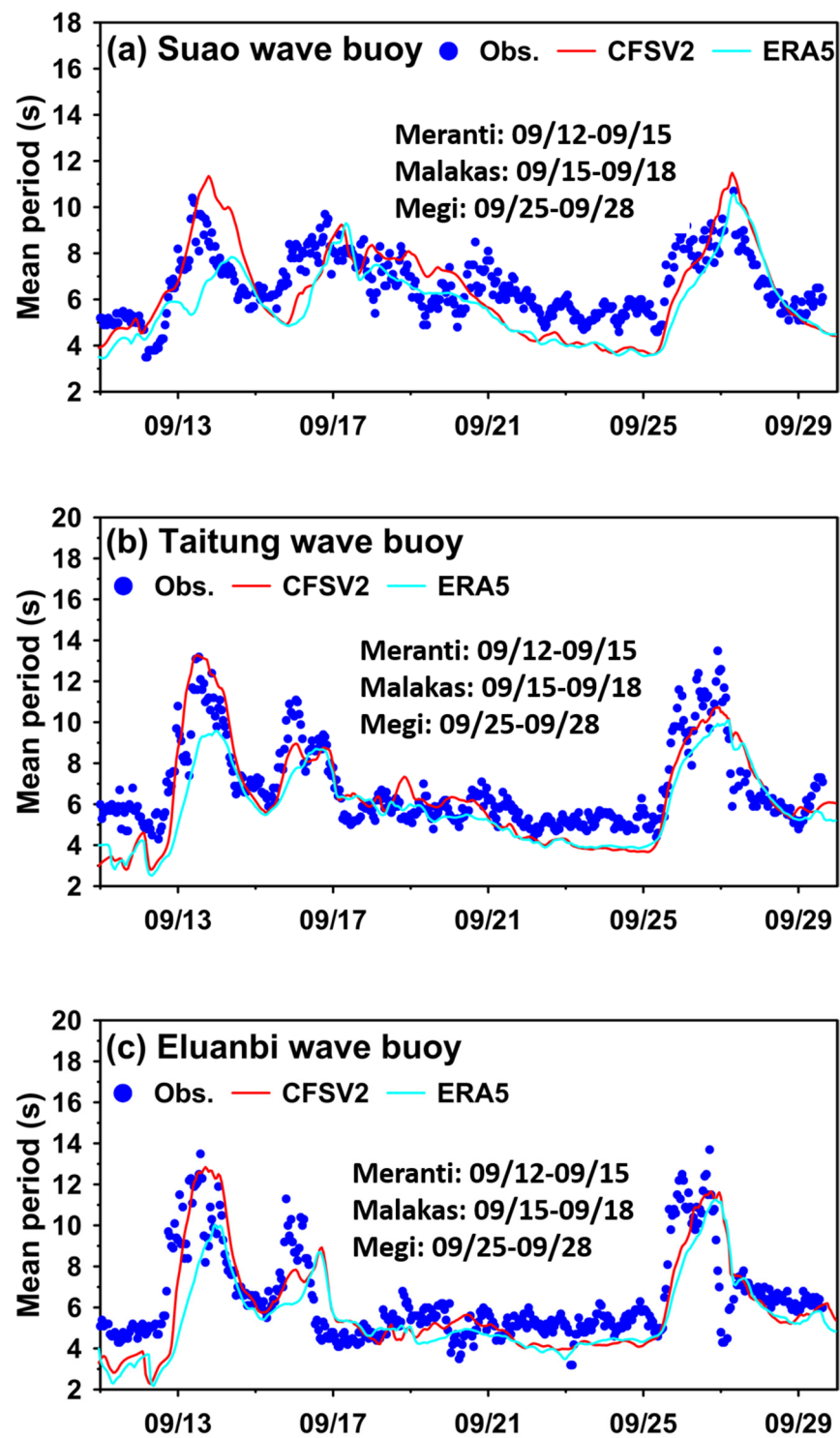
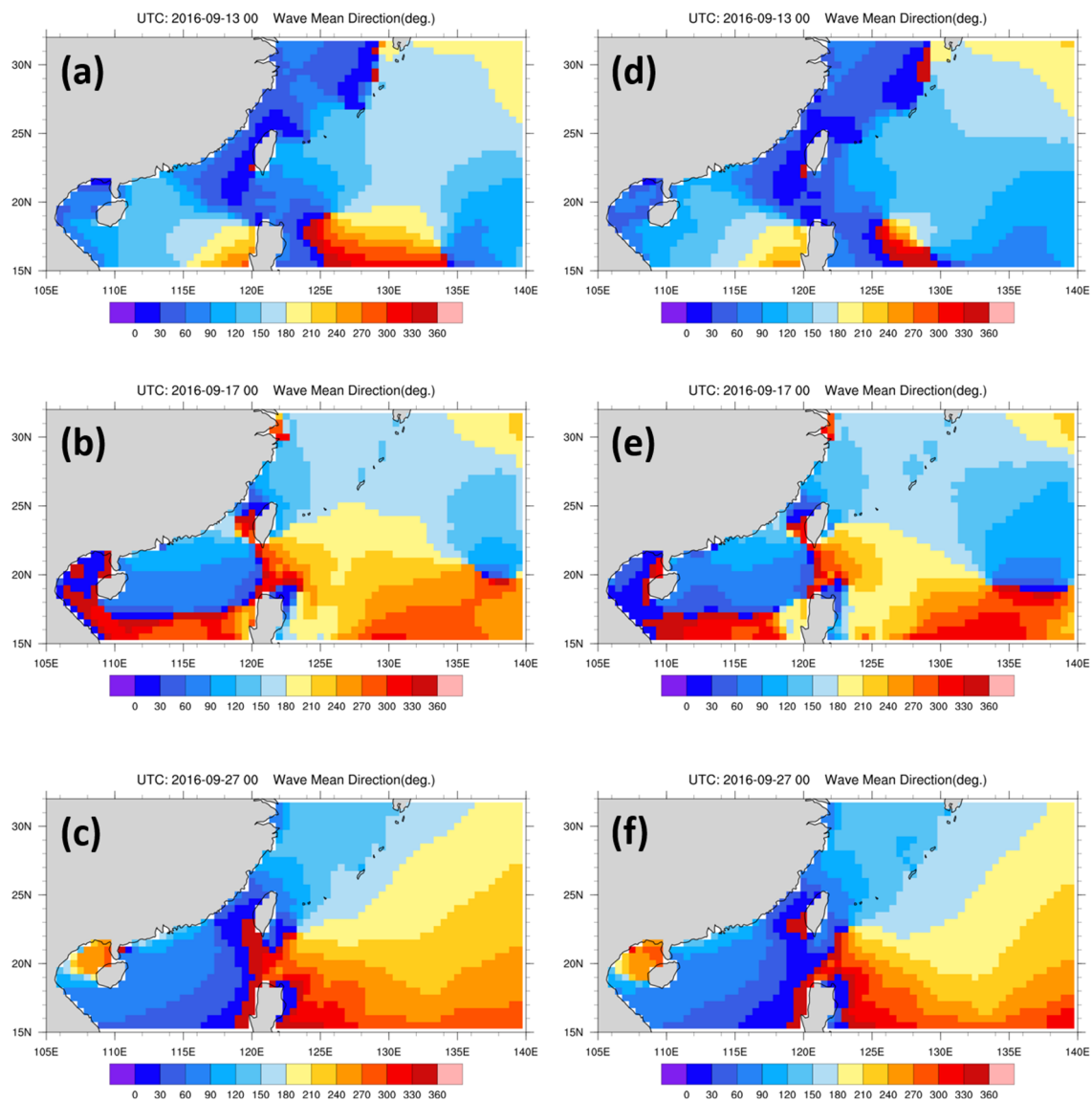


Figure 5. Comparison of the hourly mean period between simulations and measurements for the (a) Suao, (b) Taitung, and (c) Eluanbi wave buoys in September 2016.



**Figure 6.** Spatial distribution of wave direction driven by the CFSv2 (a–c) and the ERA5 (d–f) winds; a WW3 model with a 0.50 deg grid resolution was used for Typhoons Meranti (a,d), Malakas (b,e), and Megi (c,f).

#### 4.2. Accuracy of the Ocean Wave Simulation: Contributions of the Model Grid Resolutions

Since the CFSv2 winds in the WW3 model exhibited high-reliability wave parameter simulations overall compared with the ERA5 winds, the present numerical investigations use the CFSv2 winds to better understand the influence of grid resolution on typhoon wave simulations. Figure 7 delineates the instantaneous spatial distribution of the significant wave height in the deep offshore ocean caused by Typhoon Meranti using the WW3 model with 0.5 deg (Figure 7a), 0.25 deg (Figure 7b), 0.20 deg (Figure 7c), and 0.10 deg (Figure 7d) grid resolutions. The WW3 model could capture extremely significant wave heights exceeding 15.0 m in the deep nearshore ocean induced by Typhoon Meranti, even if used with different grid resolutions.

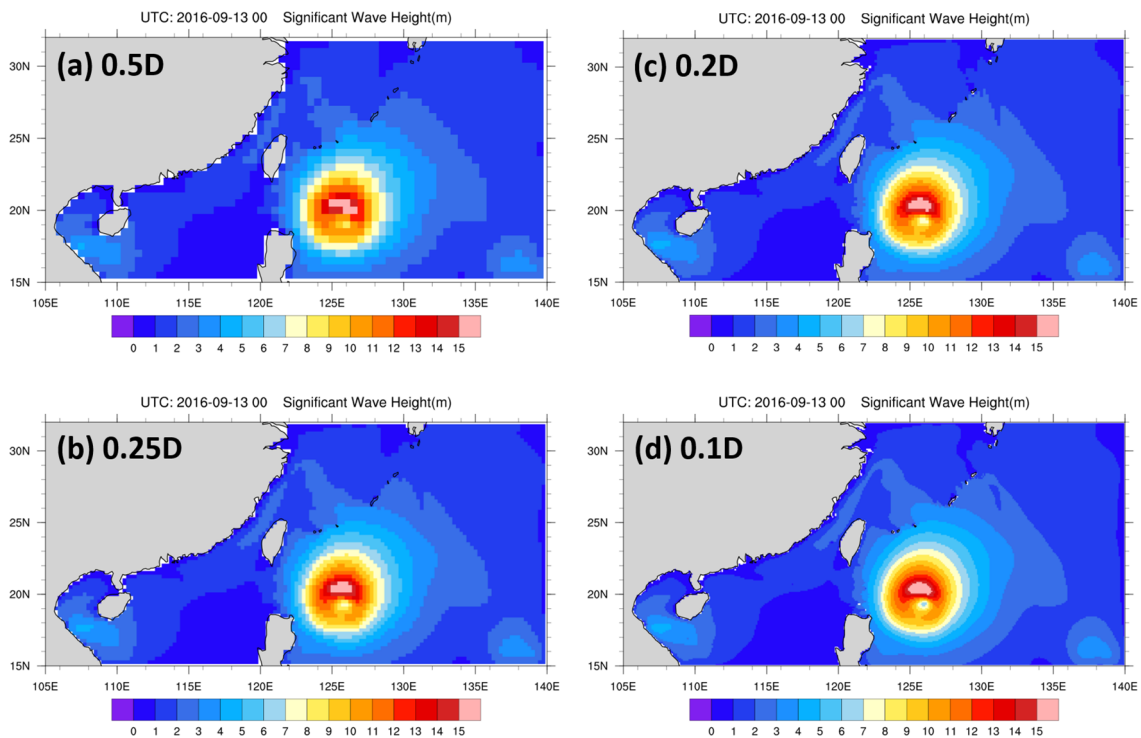


**Figure 7.** Spatial distribution of Typhoon Meranti significant wave height driven by CFSv2 using the WW3 model with (a) 0.5 deg, (b) 0.25 deg, (c) 0.2 deg, and (d) 0.1 deg grid resolutions.

The WW3 model with four grid resolutions generated similar significant wave height distributions. With the eye of the typhoon as the center, the extent of gigantic waves (>6.0 m) on the periphery is similar among the four grid resolutions. The significant difference is that the two-dimensional wave map is grid-like, uses a spatial low-resolution simulation, and is particularly obvious at grid resolutions lower than 0.25 deg. Figures 8 and 9 illustrate the instantaneous spatial distribution of the significant wave height in the deep offshore ocean caused by Typhoons Malakas and Megi, respectively, applying the WW3 model with 0.5 deg (Figures 8a and 9a), 0.25 deg (Figures 8b and 9b), 0.20 deg (Figures 8c and 9c), and 0.10 deg (Figures 8d and 9d) grid resolutions. The spatial distributions of significant wave heights are consistent when using the WW3 model with different grid resolutions, except for the grid-like appearance (Figures 8a and 9a) when adopting the WW3 model with lower grid resolutions.

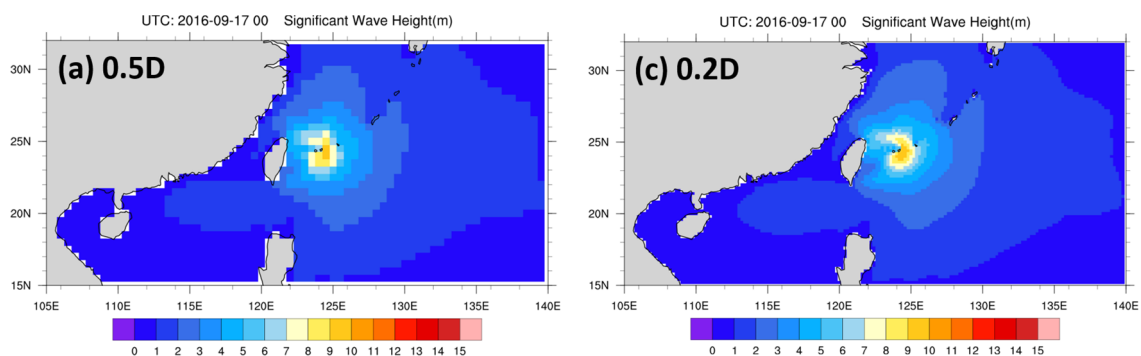


**Figure 8.** Cont.

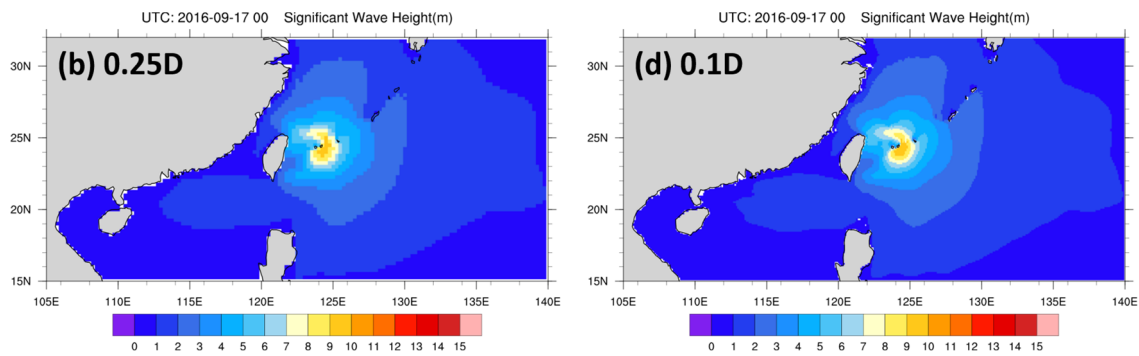


**Figure 8.** Spatial distribution of Typhoon Malakas significant wave height driven by CFSv2 using the WW3 model with (a) 0.50 deg, (b) 0.25 deg, (c) 0.20 deg, and (d) 0.10 deg grid resolutions.

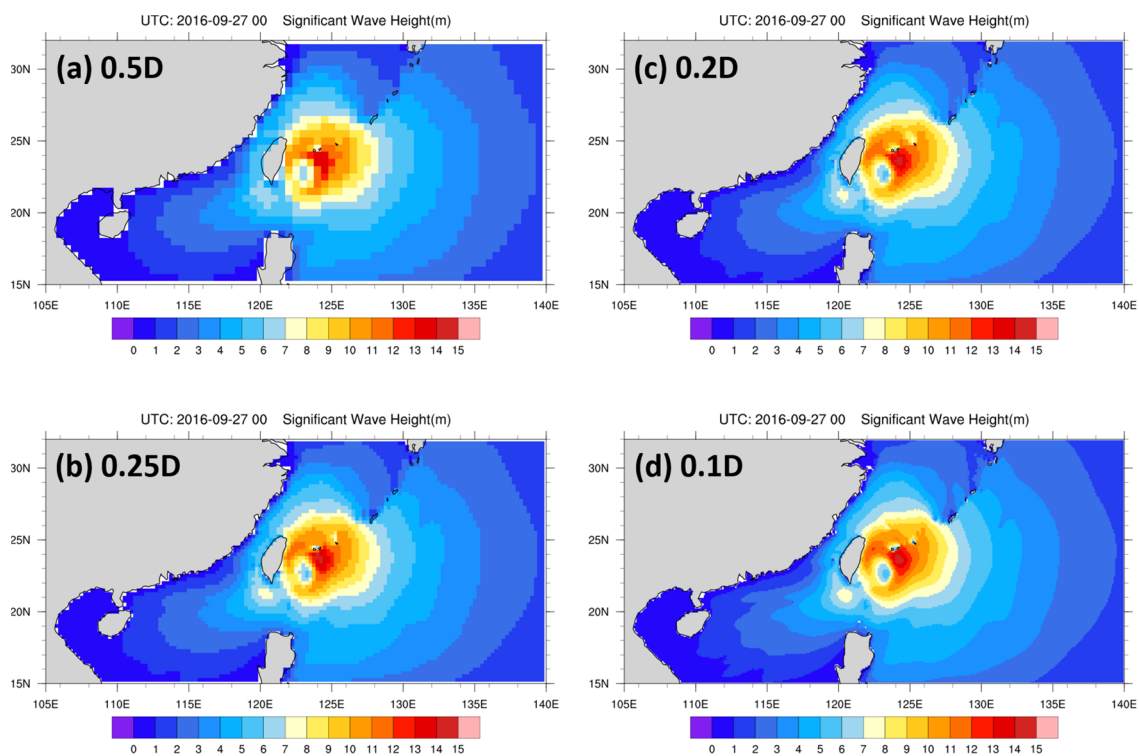


**Figure 9.** Spatial distribution of Typhoon Megi significant wave height driven by CFSv2 using the WW3 model with (a) 0.50 deg, (b) 0.25 deg, (c) 0.20 deg, and (d) 0.10 deg grid resolutions.

Figures 10 and 11 present hourly significant wave height and mean wave period comparisons at the three wave buoys using the WW3 model with different grid resolutions. The use of the WW3 model with higher resolutions (0.2 deg and 0.1 deg) captured the extremely significant wave heights that exceeded 12.0 m at the Suao wave buoy (Figure 10a) and approximately 18.0 m at the Eluanbi wave buoy (Figure 10c); however, the model still underestimated the maximum significant wave height (exceeding 15.0 m) at the Taitung wave buoy (Figure 10b), which occurred during Typhoon Meranti. Because high-resolution bathymetry needs to be improved in nearshore sea areas, the wind field away from the typhoon center might need to be more accurate. Similar phenomena were found in the mean wave period comparison (Figure 11), but the differences among the four grid resolutions were apparent at the Suao wave buoy (Figure 11c).

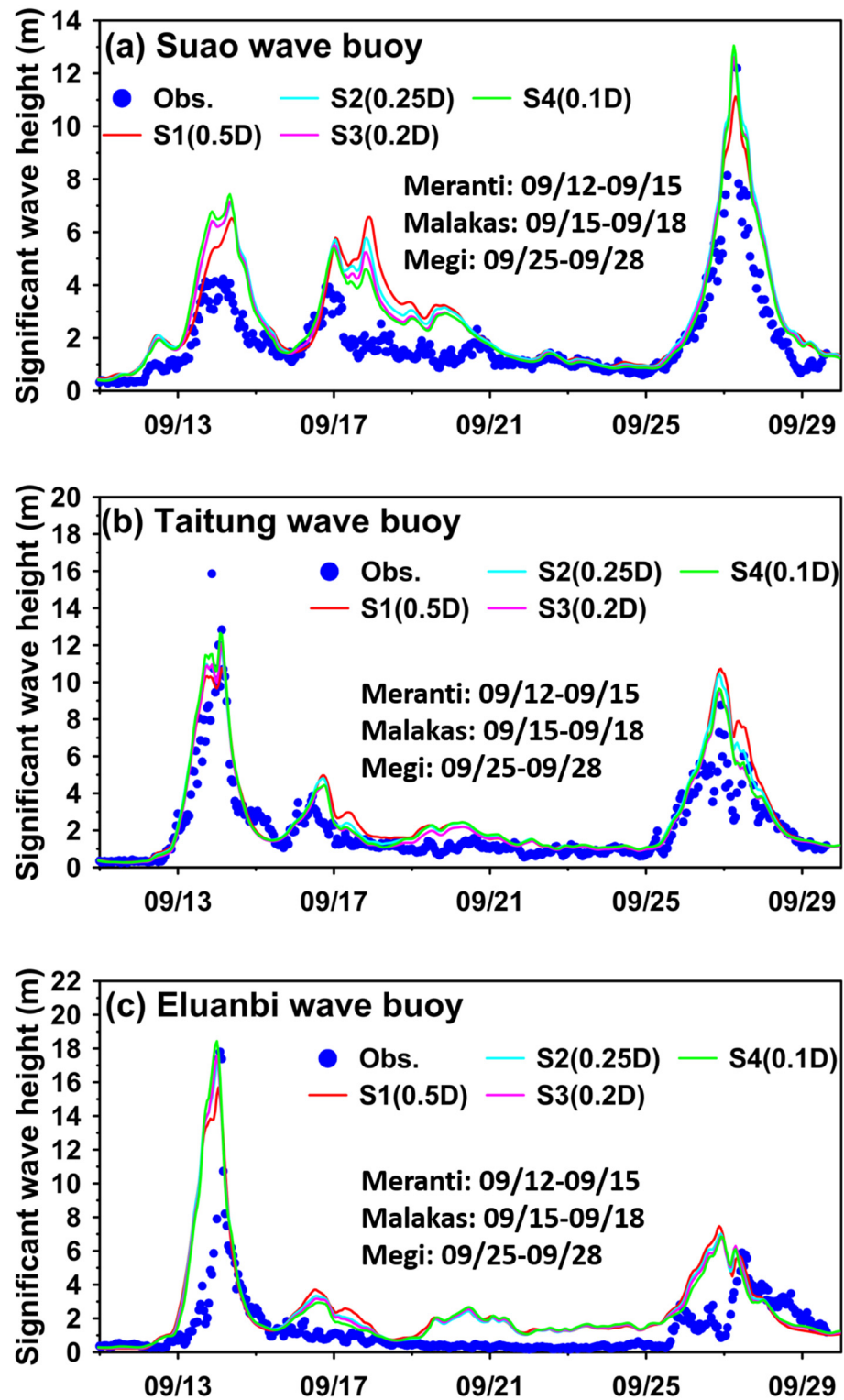


Figure 10. Comparison of the hourly significant wave heights between simulations with different grid resolutions and measurements for the (a) Suao, (b) Taitung, and (c) Eluanbi wave buoys in September 2016.

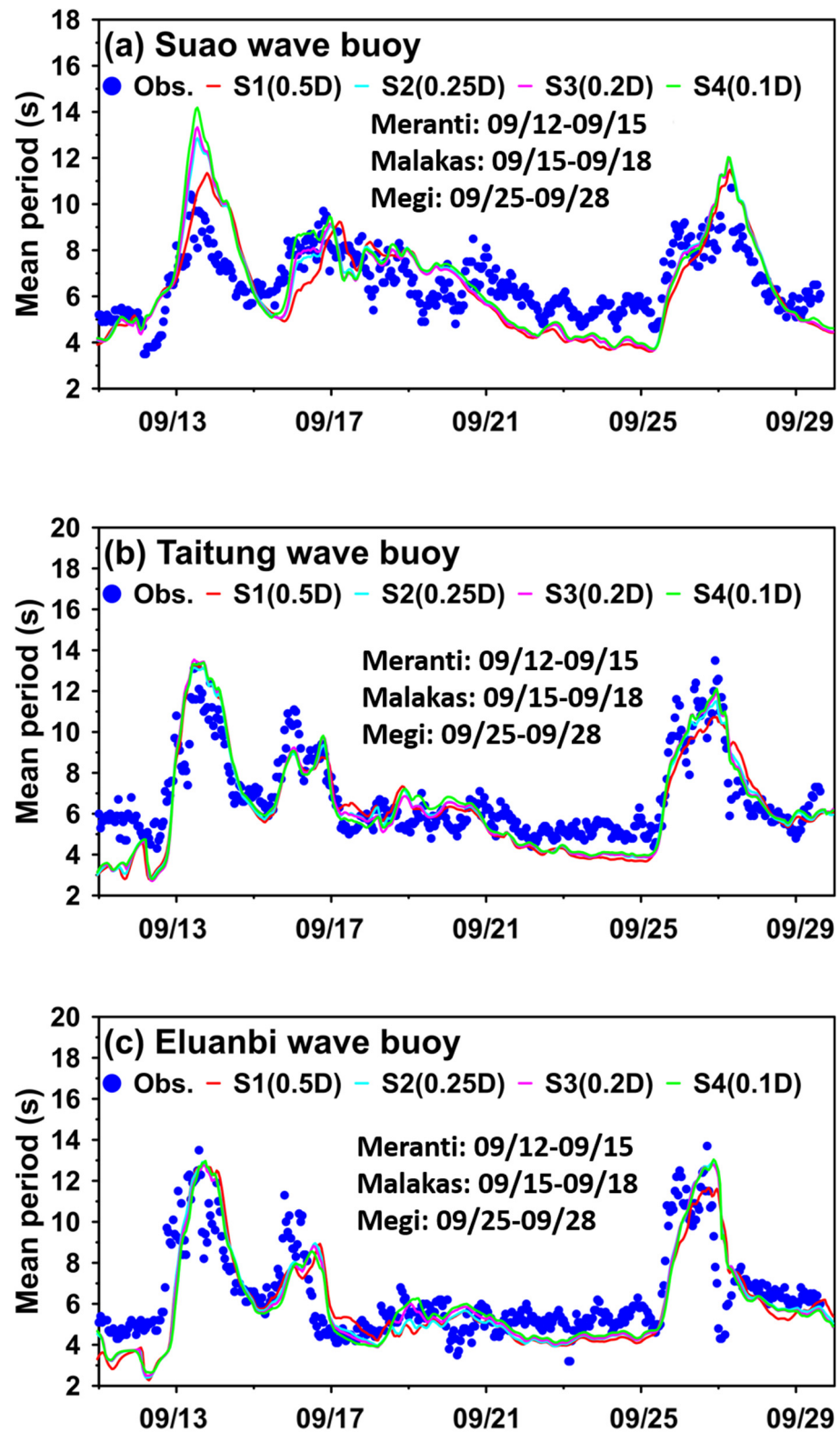


Figure 11. Comparison of the hourly mean period between simulations with different grid resolutions and measurements for the (a) Suao, (b) Taitung, and (c) Eluanbi wave buoys in September 2016.

#### 4.3. Accuracy of the Ocean Wave Simulation: Contribution of the Nonlinear Interactions

Nonlinear wave–wave interactions redistribute wave energy across the spectrum due to an exchange of energy resulting from resonant sets of wave components. Holthuijsen [35] explained the principle of nonlinear wave–wave interactions well. Two processes are

important for including nonlinear wave–wave interactions in wave models: four-wave interactions in deep and intermediate waters (known as quadruplets) and three-wave interactions in shallow waters (known as triads).

Quadruplets transfer wave energy from peak to lower frequencies in deep water; in contrast, triads transfer energy from lower to higher frequencies and transform single-peaked spectra into multiple-peaked spectra as they approach the shore. Third-generation, phase-resolved wave models include them as source terms and are computationally expensive. Nevertheless, wave model simulations often omit triads, whereas they usually consider quadruplets. Nonlinear wave–wave interactions can be modeled using the discrete interaction approximation (DIA, Refs. [33,36]), and the DIA for nonlinear resonant four-wave interactions has been at the core of third-generation wind–wave models for several decades [37]. The six scenario simulations, i.e., the WW3 model with 0.25 deg, 0.20 deg, and 0.05 deg, and exclusion and inclusion of nonlinear wave–wave interactions, investigated the effect of nonlinear wave–wave interactions on modeling the significant wave height in typhoon conditions.

Figure 12 shows a comparison of the hourly significant wave height simulation when excluding and including the wave–wave nonlinear interactions using the WW3 model with 0.25 deg (Figure 12a–c), 0.10 deg (Figure 12d–f), and 0.05 deg (Figure 12g–i) grid resolutions for the Suao (Figure 12a,d,g), Taitung (Figure 12b,e,h), and Eluanbi (Figure 12c,f,i) wave buoys (buoy locations are shown in Figure 1d). The cyan lines in Figure 12 represent the best linear regression between the wave height simulation with and without wave–wave interaction. The results show that the WW3 model consistently underestimated the significant wave heights if the model ignored the wave–wave nonlinear interactions. The underestimations worsened when the significant wave heights became large (exceeding 6 m). The maximal simulation underestimations without the wave–wave nonlinear interactions reached approximately 9.5 m for the Eluanbi wave buoy (shown in Figure 12i); this phenomenon is also notable when using a WW3 model with higher grid resolution. For instance, the maximal difference in the significant wave height simulations could be 6.5, 7.5, and 8.5 m when using the WW3 model with 0.25 deg (Figure 12b), 0.10 deg (Figure 12e), and 0.05 deg (Figure 12h) grid resolutions, respectively, for the Taitung wave buoy.

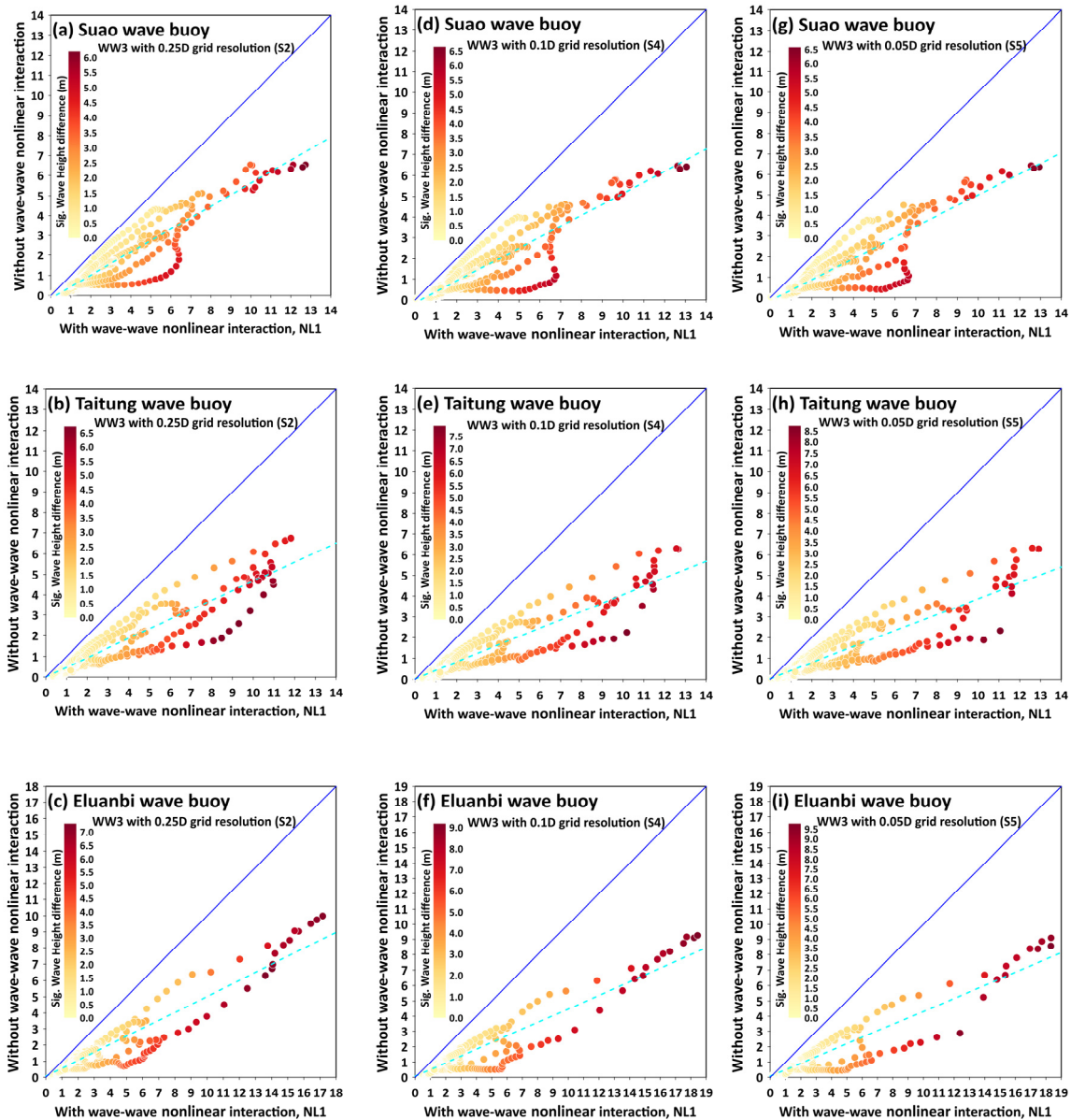


**Figure 12.** Comparison of the hourly significant wave height simulation when excluding and including the wave–wave nonlinear interaction using the WW3 model with 0.25 deg (a–c), 0.10 deg (d–f), and 0.05 deg (g–i) grid resolutions for (a,d,g) the Suao, (b,e,f) Taitung, and (c,f,i) Eluanbi wave buoys. The cyan lines represent the best linear regression between the wave height simulation with and without wave–wave interaction.

## 5. Discussion

### 5.1. Accuracy of the Ocean Wave Simulation: Contribution of the Nonlinear Interactions

The WW3 model with higher grid resolutions was more accurate for the significant wave height simulations (Figure 10), especially for typhoon-driven extreme waves. However, the significant wave height simulations tended to be identical when grid resolutions were finer than 0.2 deg. This finding is important because elapsed time is another fundamental element, in addition to accuracy, for disaster prevention. Figure 13 demonstrates the elapsed time of a 29-day simulation when using the WW3 model with 0.5 deg, 0.25 deg, 0.20 deg, 0.10 deg, and 0.05 deg grid resolutions on a 64-core computer cluster. The elapsed time increases dramatically when increasing the grid resolution, and the maximal extra elapsed time could reach 115 times when comparing the elapsed time of the WW3 model with the 0.5 deg and 0.05 deg grid resolutions. The two-dimensional contour maps of

wave parameters using the WW3 model with 0.10 deg and 0.05 deg grid resolutions for the three typhoons indicate that the simulations are nearly identical in terms of significant wave heights (Figure 14), mean periods (Figure 15), and wave directions (Figure 16). The simulation differences in the nearshore wave buoys are within 0.8 m, 0.6 s, and 20 degrees for the significant wave height, mean period, and wave direction, respectively (Figure 17). Considering immediacy and good forecasting, the WW3 model with 0.10 deg grid resolution is an optimal operational wind–wave model for Taiwanese waters because its elapsed computational time is only 0.46% compared with the actual time.

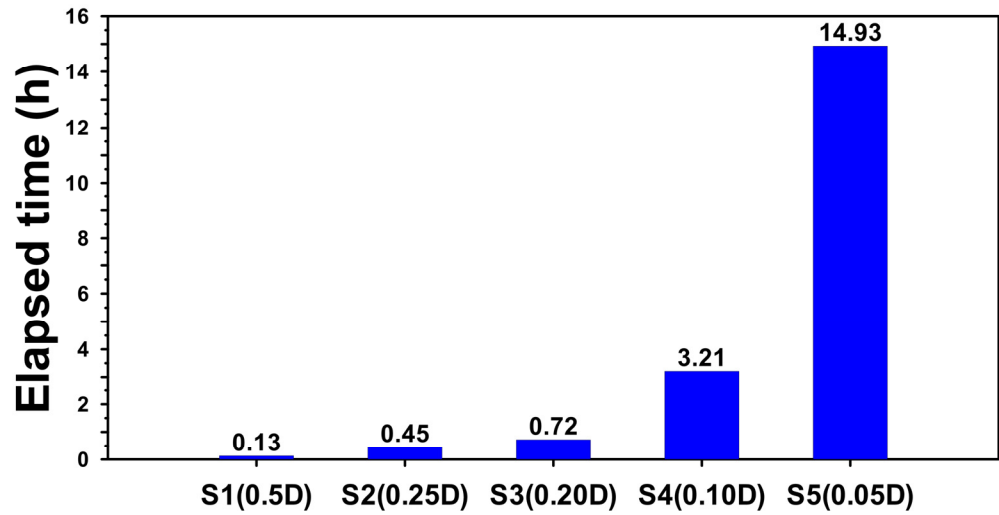


Figure 13. Elapsed time of a 29-day simulation using five model grid resolutions.

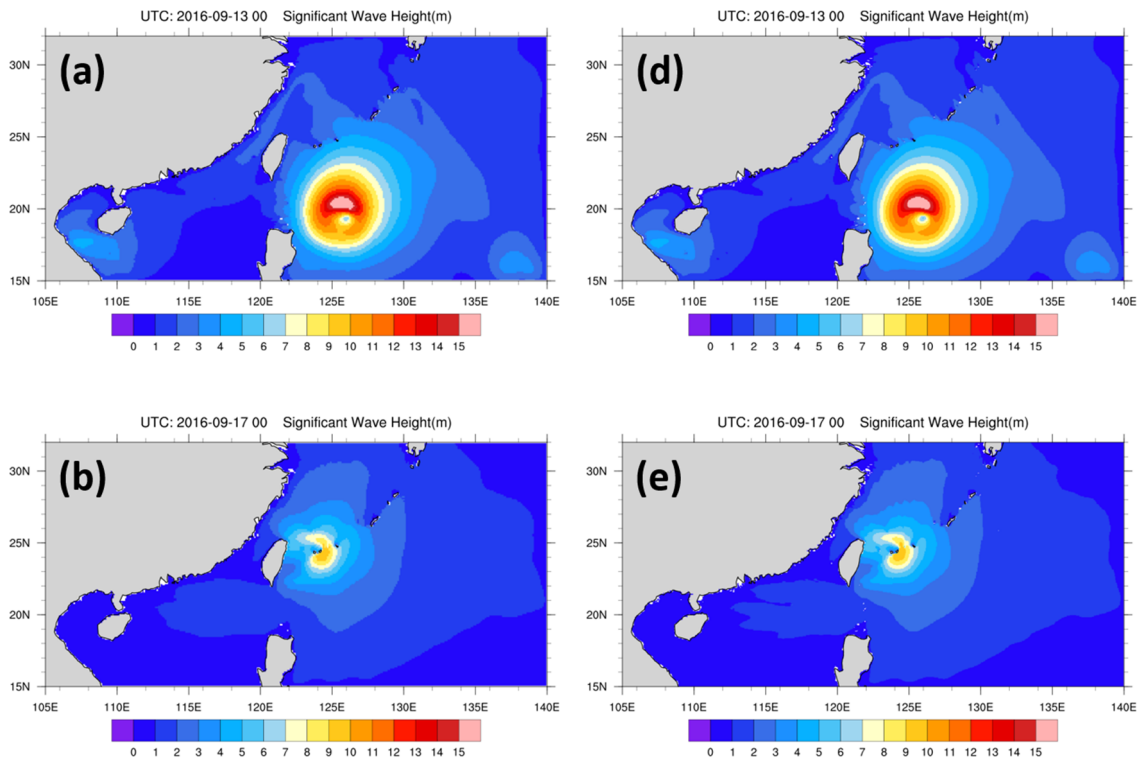
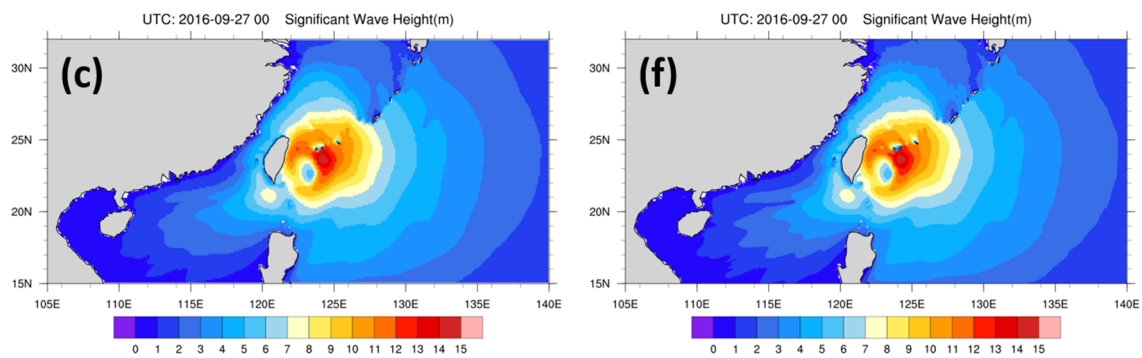
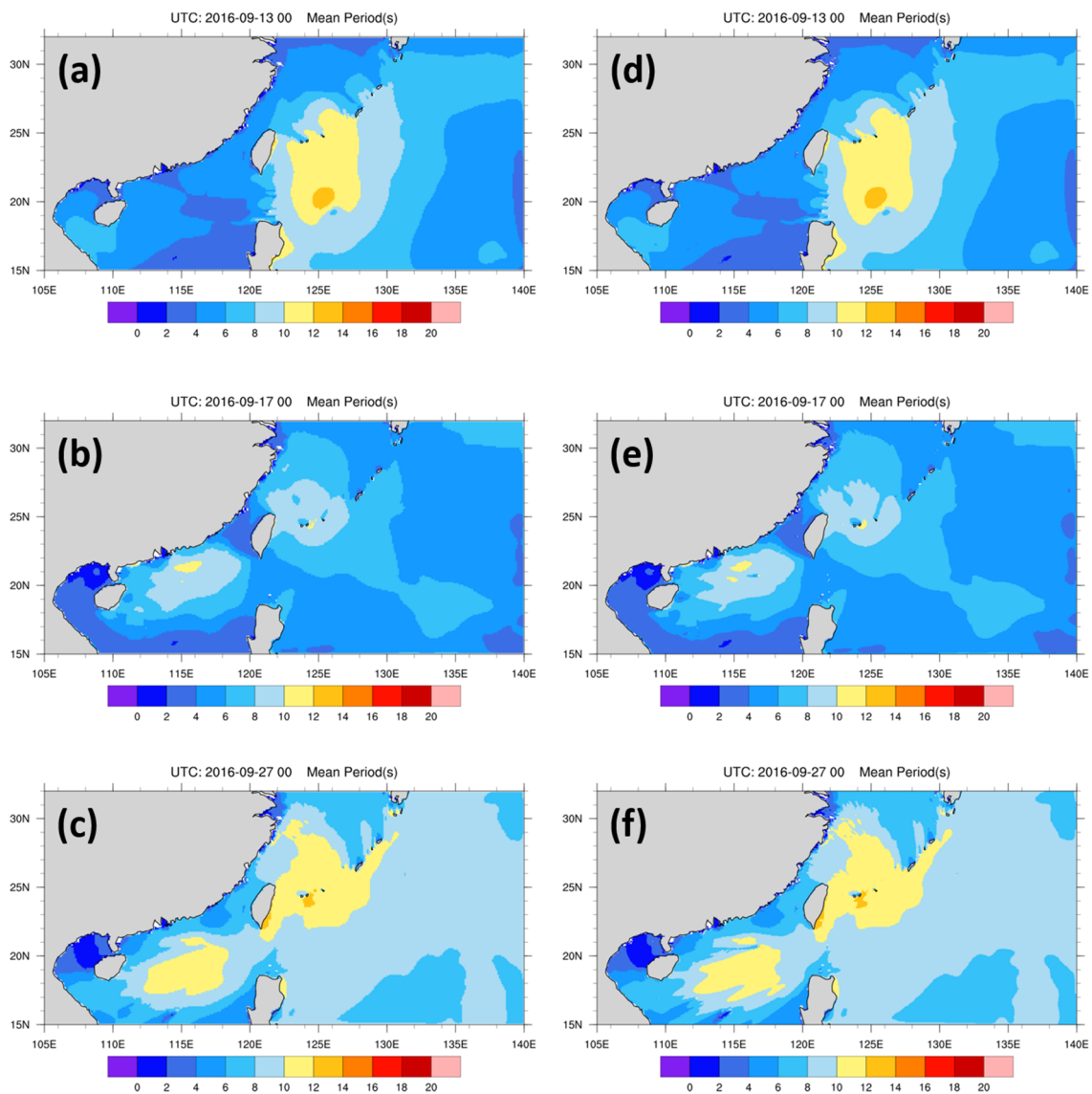


Figure 14. Cont.



**Figure 14.** Spatial distribution of significant wave heights driven by the CFSv2 using the WW3 model with 0.10 deg (a–c) and 0.05 deg grid resolutions for Typhoons Meranti (a,d), Malakas (b,e), and Megi (c,f).



**Figure 15.** Spatial distribution of the mean period driven by CFSv2 using the WW3 model with 0.1 deg (a–c) and 0.05 deg grid resolutions for Typhoons Meranti (a,d), Malakas (b,e), and Megi (c,f).

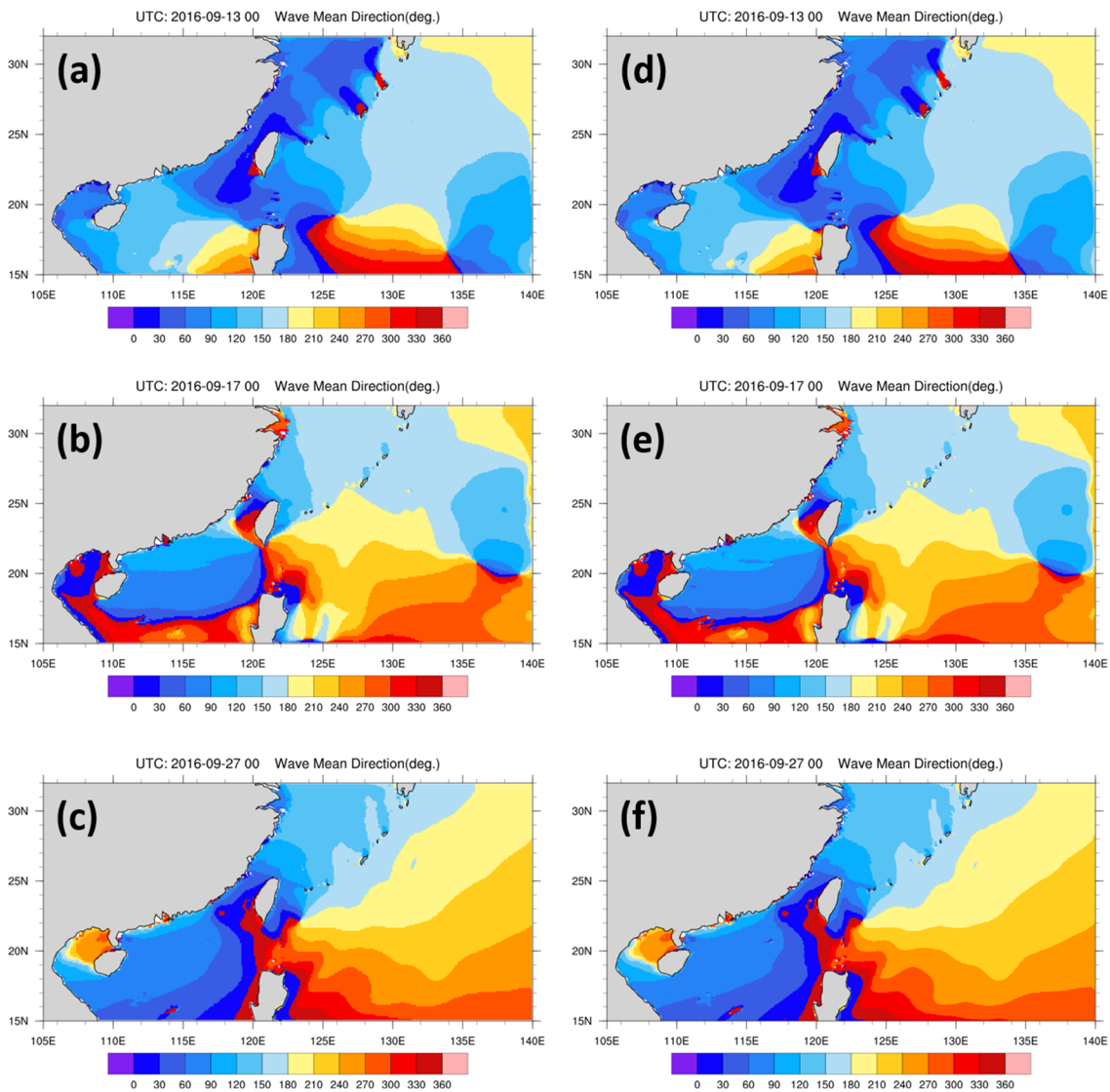


Figure 16. Spatial distribution of wave direction driven by the CFSv2 using the WW3 model with 0.1 deg (a–c) and 0.05 deg grid resolutions for Typhoons Meranti (a,d), Malakas (b,e), and Megi (c,f).

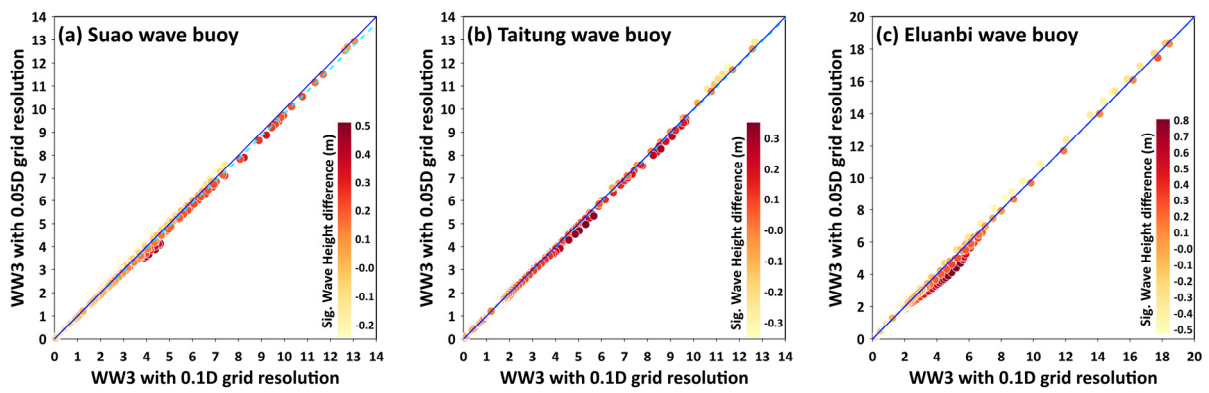
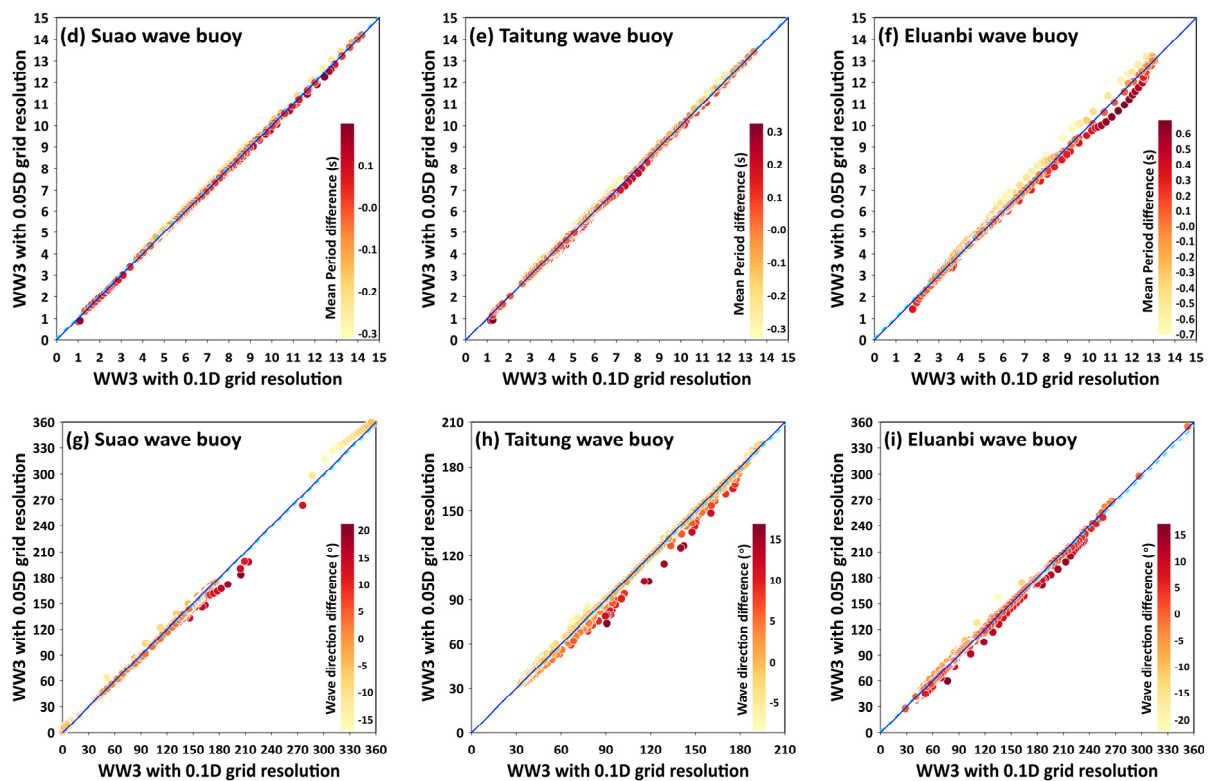


Figure 17. Cont.



**Figure 17.** Comparison of the hourly significant wave height (a–c), mean period (d–f), and wave direction (g–i) simulated by the WW3 model with 0.10 deg and 0.05 deg grid resolutions for the (a,d,g) Suao, (b,e,h) Taitung, and (c,f,i) Eluanbi wave buoys.

### 5.2. Intercomparison of the WW3 and WWM-III Models for Typhoon Wave Simulations

A state-of-the-art, third-generation, unstructured-grid Wind Wave Model III (WWM-III, Ref. [22]) was implemented to compare three successive typhoon-induced significant wave heights and mean periods among the models. The size of the computational domain is identical to that of the WW3 model implemented in the present study. More details about the WWM-III configurations can be found in [5–7,29,38]. Although the use of a blended wind (a combination of dynamic and parametric winds) could lead to more accurate typhoon wave simulations [2–5,39,40], the CFSv2 winds were used with the WWM-III to make the simulation results comparable to those of the WW3 model with a 0.10 deg grid resolution. Figure 18 illustrates the intercomparison of significant wave height (Figure 18a–c) and mean period (Figure 18d–f) simulations using the third-generation models WW3 (with a 0.1 deg grid resolution) and WWM-III. The comparisons show that the WWM-III model tends to overestimate significant wave heights and mean periods, which is particularly obvious during the passage of extreme typhoon waves at wave buoys. Overall, the WW3 model predicted more accurate wave parameters than those derived from the WWM-III model for the three successive typhoons in the present study.

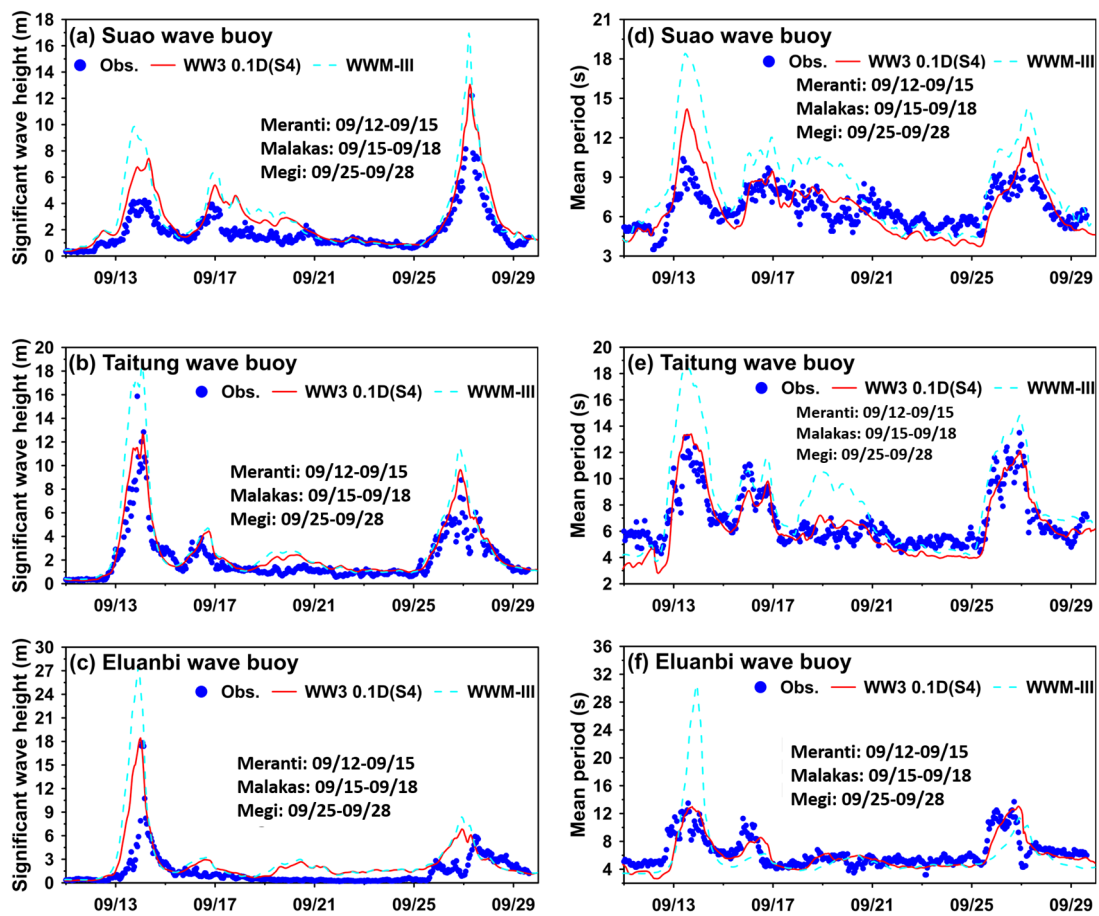


**Figure 18.** Comparison of the hourly significant wave height (a–c) and mean period (d–f) simulations using the WW3 (0.1D) and WWM-III models for the (a,d) Suao, (b,e) Taitung, and (c,f) Eluanbi wave buoys.

### 6. Summary and Conclusions

In this study, the significant wave heights, mean wave periods, and wave directions in the waters surrounding Taiwan in September 2016 were reproduced, covering Typhoons Meranti, Malakas, and Megi, by applying a state-of-the-art, third-generation wind–wave model, WAVEWATCH III (WW3) version 6.07. The typhoon’s wind fields from the CFS version 2 (CFSv2) of the NCEP and ERA5 of the ECMWF were used as the meteorological conditions for the WW3 model with a sizeable computational domain and 0.5 deg grid resolution to achieve excellent simulation performances. The CFSv2 winds were used to investigate the contributions of the model’s grid resolutions to the wave parameters for the three successive typhoons that impacted Taiwan in September 2016 because the maximum significant wave height simulations were well matched by the application of the CFSv2 winds.

Five grid resolutions (0.5 deg, 0.25 deg, 0.20 deg, 0.10 deg, and 0.05 deg) with the same computational domain were created and used in the WW3 model to investigate the contributions of grid resolutions to wave parameter simulation during the three successive typhoons that impacted Taiwan in September 2016. The comparisons indicated that the WW3 model with higher grid resolutions is more accurate for significant wave height simulations, particularly for typhoon-driven extreme waves. However, the simulations were more identical when grid resolutions were finer than 0.20 deg. Considering efficiency and accuracy, the WW3 model with a 0.10 deg grid resolution is an optimal operational wind–wave model for Taiwanese waters because its computer-elapsed time is only 3.21 h for a 29-day simulation. Additionally, supposing the wave–wave nonlinear interactions are excluded from the WW3 model, the maximal underestimations of typhoon-driven waves

would be notable when the significant wave heights exceed 6 m. The underestimations would worsen using a WW3 model with a higher grid resolution.

The intercomparison of wave parameter simulations in September 2016 for Taiwanese waters was conducted using two third-generation models, the unstructured-grid-based WWM-III and the WW3 with a 0.10 deg grid resolution. Overall, the intercomparisons show that the WWM-III model overestimated the significant wave heights and mean periods during extreme typhoon waves at the wave buoys. Moreover, the present study also reveals that the WW3 model predicted more accurate wave parameters than those computed by the WWM-III model for the three successive typhoons. However, long-term measurements of wave parameters in deep and coastal Taiwanese waters should be adopted to validate and intercompare the performances of the WW3 and WWM-III models. Amid ongoing climate change, which amplifies storm wave risks from successive typhoon events, researchers and scientists should apply an appropriate wind–wave model to obtain more accurate forecasts and projections to protect coastal communities facing potential disasters.

**Author Contributions:** S.-C.H.: investigation, conceptualization, methodology, software, visualization, and writing. H.-L.W.: visualization and writing—review and editing. W.-B.C.: investigation, conceptualization, software, and writing—review and editing. All authors have read and agreed to the published version of the manuscript.

**Funding:** This research was supported by the National Science and Technology Council (NSCT), Taiwan, grant no. MOST 111-2221-E-865-001.

**Institutional Review Board Statement:** Not applicable.

**Informed Consent Statement:** Not applicable.

**Data Availability Statement:** Publicly available datasets were analyzed in the present study. The data can be found here: <https://ocean.cwb.gov.tw/V2/>, accessed on 19 March 2023.

**Acknowledgments:** The authors would like to thank the Water Resource Agency in Taiwan and the National Oceanic and Atmospheric Administration in the United States for providing the wave buoy measurements and WAVEWATCH III, respectively.

**Conflicts of Interest:** The authors declare no conflict of interest.

## References

1. Balaguru, K.; Foltz, G.R.; Leung, L.R.; Emanuel, K.A. Global warming-induced upper-ocean freshening and the intensification of super typhoons. *Nat. Commun.* **2016**, *7*, 13670. [[CrossRef](#)] [[PubMed](#)]
2. Chang, T.-Y.; Chen, H.; Hsiao, S.-C.; Wu, H.-L.; Chen, W.-B. Numerical Analysis of the Effect of Binary Typhoons on Ocean Surface Waves in Waters Surrounding Taiwan. *Front. Mar. Sci.* **2021**, *8*, 749185. [[CrossRef](#)]
3. Chang, C.-H.; Shih, H.-J.; Chen, W.-B.; Su, W.-R.; Lin, L.-Y.; Yu, Y.-C.; Jang, J.-H. Hazard Assessment of Typhoon-Driven Storm Waves in the Nearshore Waters of Taiwan. *Water* **2018**, *10*, 926. [[CrossRef](#)]
4. Chen, W.-B.; Chen, H.; Hsiao, S.-C.; Chang, C.-H.; Lin, L.-Y. Wind forcing effect on hindcasting of typhoon-driven extreme waves. *Ocean Eng.* **2019**, *188*, 106260. [[CrossRef](#)]
5. Hsiao, S.-C.; Chen, H.; Wu, H.-L.; Chen, W.-B.; Chang, C.-H.; Guo, W.-D.; Chen, Y.-M.; Lin, L.-Y. Numerical Simulation of Large Wave Heights from Super Typhoon Nepartak (2016) in the Eastern Waters of Taiwan. *J. Mar. Sci. Eng.* **2020**, *8*, 217. [[CrossRef](#)]
6. Hsiao, S.-C.; Wu, H.-L.; Chen, W.-B.; Chang, C.-H.; Lin, L.-Y. On the Sensitivity of Typhoon Wave Simulations to Tidal Elevation and Current. *J. Mar. Sci. Eng.* **2020**, *8*, 731. [[CrossRef](#)]
7. Hsiao, S.-C.; Wu, H.-L.; Chen, W.-B.; Guo, W.-D.; Chang, C.-H.; Su, W.-R. Effect of Depth-Induced Breaking on Wind Wave Simulations in Shallow Nearshore Waters off Northern Taiwan during the Passage of Two Super Typhoons. *J. Mar. Sci. Eng.* **2021**, *9*, 706. [[CrossRef](#)]
8. Shao, Z.; Liang, B.; Li, H.; Wu, G.; Wu, Z. Blended wind fields for wave modeling of tropical cyclones in the South China Sea and East China Sea. *Appl. Ocean Res.* **2018**, *71*, 20–33. [[CrossRef](#)]
9. Shih, H.-J.; Chen, H.; Liang, T.-Y.; Fu, H.-S.; Chang, C.-H.; Chen, W.-B.; Su, W.-R.; Lin, L.-Y. Generating potential risk maps for typhoon-induced waves along the coast of Taiwan. *Ocean Eng.* **2018**, *163*, 1–14. [[CrossRef](#)]
10. Liang, T.-Y.; Chang, C.-H.; Hsiao, S.-C.; Huang, W.-P.; Chang, T.-Y.; Guo, W.-D.; Liu, C.-H.; Ho, J.-Y.; Chen, W.-B. On-Site Investigations of Coastal Erosion and Accretion for the Northeast of Taiwan. *J. Mar. Sci. Eng.* **2022**, *10*, 282. [[CrossRef](#)]
11. Choi, Y.; Cha, D.; Lee, M.; Kim, J.; Jin, C.; Park, S.; Joh, M. Satellite radiance data assimilation for binary tropical cyclone cases over the western North Pacific. *J. Adv. Model. Earth Syst.* **2017**, *9*, 832–853. [[CrossRef](#)]

12. Jang, W.; Chun, H.-Y. Characteristics of Binary Tropical Cyclones Observed in the Western North Pacific for 62 Years (1951–2012). *Mon. Weather. Rev.* **2015**, *143*, 1749–1761. [[CrossRef](#)]
13. Khain, A.; Ginis, I.; Falkovich, A.; Frumin, M. Interaction of binary tropical cyclones in a coupled tropical cyclone-ocean model. *J. Geophys. Res. Atmos.* **2000**, *105*, 22337–22354. [[CrossRef](#)]
14. Wu, X.; Fei, J.; Huang, X.; Zhang, X.; Cheng, X.; Ren, J. A numerical study of the interaction between two simultaneous storms: Goni and Morakot in September 2009. *Adv. Atmos. Sci.* **2012**, *29*, 561–574. [[CrossRef](#)]
15. Yang, C.-C.; Wu, C.-C.; Chou, K.-H.; Lee, C.-Y. Binary Interaction between Typhoons Fengshen (2002) and Fungwong (2002) Based on the Potential Vorticity Diagnosis. *Mon. Weather. Rev.* **2008**, *136*, 4593–4611. [[CrossRef](#)]
16. Cavaleri, L.; Alves, J.-H.; Ardhuin, F.; Babanin, A.; Banner, M.; Belibassakis, K.; Benoit, M.; Donelan, M.; Groeneweg, J.; Herbers, T.; et al. Wave modelling—The state of the art. *Prog. Oceanogr.* **2007**, *75*, 603–674. [[CrossRef](#)]
17. Abdolali, A.; Van Der Westhuysen, A.; Ma, Z.; Mehra, A.; Roland, A.; Moghimi, S. Evaluating the accuracy and uncertainty of atmospheric and wave model hindcasts during severe events using model ensembles. *Ocean Dyn.* **2021**, *71*, 217–235. [[CrossRef](#)]
18. Powell, M.D.; Murillo, S.; Dodge, P.; Uhlhorn, E.; Gamache, J.; Cardone, V.; Cox, A.; Otero, S.; Carrasco, N.; Annane, B.; et al. Reconstruction of Hurricane Katrina’s wind fields for storm surge and wave hindcasting. *Ocean Eng.* **2010**, *37*, 26–36. [[CrossRef](#)]
19. WAMDI Group. The WAM model- A third generation ocean wave prediction model. *J. Phys. Oceanogr.* **1988**, *18*, 1775–1810. [[CrossRef](#)]
20. Tolman, H.L.; Balasubramaniyan, B.; Burroughs, L.D.; Chalikov, D.V.; Chao, Y.Y.; Chen, H.S.; Gerald, V.M. Development and implementation of wind generated ocean surface wave models at NCEP. *Weather Forecast.* **2002**, *17*, 311–333. [[CrossRef](#)]
21. Booij, N.; Ris, R.C.; Holthuijsen, L.H. A third-generation wave model for coastal regions: 1. Model description and validation. *J. Geophys. Res. Oceans* **1999**, *104*, 7649–7666. [[CrossRef](#)]
22. Roland, A.; Zhang, Y.J.; Wang, H.V.; Meng, Y.; Teng, Y.-C.; Maderich, V.; Brovchenko, I.; Dutour-Sikiric, M.; Zanke, U. A fully coupled 3D wave-current interaction model on unstructured grids. *J. Geophys. Res. Oceans* **2012**, *117*, C00J33. [[CrossRef](#)]
23. Umesh, P.; Swain, J.; Balchand, A. Inter-comparison of WAM and WAVEWATCH-III in the North Indian Ocean using ERA-40 and QuikSCAT/NCEP blended winds. *Ocean Eng.* **2018**, *164*, 298–321. [[CrossRef](#)]
24. Hersbach, H.; Bell, B.; Berrisford, P.; Hirahara, S.; Horanyi, A.; Muñoz-Sabater, J.; Nicolas, J.; Peubey, C.; Radu, R.; Schepers, D.; et al. The ERA5 global reanalysis. *Q. J. R. Meteorol. Soc.* **2020**, *146*, 1999–2049. [[CrossRef](#)]
25. Saha, S.; Moorthi, S.; Wu, X.; Wang, J.; Nadiga, S.; Tripp, P.; Behringer, D.; Hou, Y.-T.; Chuang, H.-Y.; Iredell, M.; et al. The NCEP Climate Forecast System Version 2. *J. Clim.* **2014**, *27*, 2185–2208. [[CrossRef](#)]
26. GEBCO Compilation Group. *GEBCO 2022 Grid*; GEBCO Compilation Group: Liverpool, UK, 2022. [[CrossRef](#)]
27. WW3DG. User Manual and System Documentation of WAVEWATCH III Version 6.07, The WAVEWATCH III Development Group. Tech. Note 326 Pp. + Appendices, NOAA/NWS/NCEP/MMAB. 2019. College Park, MD, USA. Available online: [https://www.researchgate.net/publication/336069899\\_User\\_manual\\_and\\_system\\_documentation\\_of\\_WAVEWATCH\\_III\\_R\\_version\\_607](https://www.researchgate.net/publication/336069899_User_manual_and_system_documentation_of_WAVEWATCH_III_R_version_607) (accessed on 19 March 2023).
28. Abdolali, A.; Roland, A.; van der Westhuysen, A.; Meixner, J.; Chawla, A.; Hesser, T.J.; Smith, J.M.; Sikiric, M.D. Large-scale hurricane modeling using domain decomposition parallelization and implicit scheme implemented in WAVEWATCH III wave model. *Coast. Eng.* **2020**, *157*, 103656. [[CrossRef](#)]
29. Chen, W.-B. Typhoon Wave Simulation Responses to Various Reanalysis Wind Fields and Computational Domain Sizes. *J. Mar. Sci. Eng.* **2022**, *10*, 1360. [[CrossRef](#)]
30. Ardhuin, F.; Rogers, E.; Babanin, A.V.; Filipot, J.-F.; Magne, R.; Roland, A.; Van Der Westhuysen, A.; Queffelec, P.; Lefevre, J.-M.; Aouf, L.; et al. Semiempirical Dissipation Source Functions for Ocean Waves. Part I: Definition, Calibration, and Validation. *J. Phys. Oceanogr.* **2010**, *40*, 1917–1941. [[CrossRef](#)]
31. Hasselmann, K.; Barnett, T.P.; Bouws, E.; Carlson, H.; Cartwright, D.E.; Enke, K.; Ewing, J.A.; Gienapp, H.; Hasselmann, D.E.; Kruseman, P.; et al. *Measurements of Wind-Wave Growth and Swell Decay during the Joint North Sea Wave Project (JONSWAP)*; Deutsches Hydrographisches Institut: Berlin/Hamburg, Germany, 1973; Available online: <https://repository.tudelft.nl/islandora/object/uuid%3Af204e188-13b9-49d8-a6dc-4fb7c20562fc> (accessed on 19 March 2023).
32. Battjes, J.A.; Janssen, J.P.F.M. Energy loss and set-up due to breaking of random waves. *Coast. Eng. Proc.* **1978**, *1*, 32. [[CrossRef](#)]
33. Tolman, H.L. Inverse modeling of discrete interaction approximations for nonlinear interactions in wind waves. *Ocean Model.* **2004**, *6*, 405–422. [[CrossRef](#)]
34. Monteiro, N.M.; Oliveira, T.C.; Silva, P.A.; Abdolali, A. Wind-wave characterization and modeling in the Azores Archipelago. *Ocean Eng.* **2022**, *263*, 112395. [[CrossRef](#)]
35. Holthuijsen, L.H. *Waves in Oceanic and Coastal Waters*; Cambridge University Press (CUP): Cambridge, UK, 2007. [[CrossRef](#)]
36. Hasselmann, S.; Hasselmann, K.; Allender, J.H.; Barnett, T.P. Computations and parameterizations of the nonlinear energy transfer in a gravity-wave spectrum, Part II: Parameterizations of the nonlinear energy transfer for application in wave models. *J. Phys. Oceanogr.* **1985**, *15*, 1378–1391. [[CrossRef](#)]
37. Tolman, H.L. A Generalized Multiple Discrete Interaction Approximation for resonant four-wave interactions in wind wave models. *Ocean Model.* **2013**, *70*, 11–24. [[CrossRef](#)]
38. Su, W.-R.; Chen, H.; Chen, W.-B.; Chang, C.-H.; Lin, L.-Y.; Jang, J.-H.; Yu, Y.-C. Numerical investigation of wave energy resources and hotspots in the surrounding waters of Taiwan. *Renew. Energy* **2018**, *118*, 814–824. [[CrossRef](#)]

39. Hsiao, S.-C.; Chen, H.; Chen, W.-B.; Chang, C.-H.; Lin, L.-Y. Quantifying the contribution of nonlinear interactions to storm tide simulations during a super typhoon event. *Ocean Eng.* **2019**, *194*, 106661. [[CrossRef](#)]
40. Yu, Y.-C.; Chen, H.; Shih, H.-J.; Chang, C.-H.; Hsiao, S.-C.; Chen, W.-B.; Chen, Y.-M.; Su, W.-R.; Lin, L.-Y. Assessing the Potential Highest Storm Tide Hazard in Taiwan Based on 40-Year Historical Typhoon Surge Hindcasting. *Atmosphere* **2019**, *10*, 346. [[CrossRef](#)]

**Disclaimer/Publisher's Note:** The statements, opinions and data contained in all publications are solely those of the individual author(s) and contributor(s) and not of MDPI and/or the editor(s). MDPI and/or the editor(s) disclaim responsibility for any injury to people or property resulting from any ideas, methods, instructions or products referred to in the content.